F. Yamashita[1], E. Fukuyama[2,1], and S. Xu[3]

[1] National Research Institute for Earth Science and Disaster Resilience.

[2] Department of Civil and Earth Resources Engineering, Kyoto University.

[3] Department of Earth and Space Sciences, Southern University of Science and Technology.

Corresponding author: Futoshi Yamashita (yamafuto@bosai.go.jp)

Key Points

- Experiments on a 4-m-long rock fault show two stages of slow slip evolution and foreshock activities preceding main fast rupture.
- Most foreshocks were triggered by the slow slip at the second stage with a rate faster than 100 µm/s regardless of accumulated slip amount.
- Magnitude of repeating foreshocks tended to positively correlate with local slip rate in three of four repeater groups.

Abstract

We report laboratory experimental results to reveal the factors that control the occurrence and magnitude of foreshocks. We conducted rock friction experiments using an apparatus that can shear 4-meter-long rock specimens. We observed many stick-slip events, as well as very slow (several tens of m/s) but long-lasting slips between those main events. These long-term slow slips individually initiated from both the leading and trailing edges of the fault, and kept propagating steadily towards each other. Such steady slips did not immediately trigger any seismic events, regardless of the accumulated slip amount. After the coalescence of the two long-term slow slip fronts, a second phase of slow slip with higher slip rate (several hundreds of m/s) — called precursory slow slip, began at the central area and was accompanied by the occurrence of small seismic events (foreshocks). Subsequently, the main fast rupture eventually developed. We propose that the asperities that hosted foreshocks had similar size to the local critical nucleation length h^*; the asperities slipped stably when the local loading rate was low, but could also slip unstably and radiated seismic waves when the local loading rate became high. We further found a clear positive correlation between foreshock magnitude and local slip rate. These results suggest that local loading rate has a significant influence on the occurrence and magnitude of foreshocks. Therefore, its effect should be taken into account during the studies of earthquake nucleation process and other similar phenomena such as Episodic Tremor and Slip (ETS), icequakes, and repeating earthquakes.

Plain Language Summary

It is known that two contacting surfaces do not perfectly fit with each other, but with very limited areas in actual contact. The real contacting areas are highly stressed and can serve as asperities — a situation thought to also apply to a natural fault. It is also considered that asperities are more difficult to break, but

can generate seismic waves once broken. However, the exact conditions when the asperities break are still unclear. To investigate them, we have conducted laboratory experiments with 4-meter-long rock blocks. We observed extremely slow (several tens of m/s) fault slips during the shear loading stage. While no seismic events occurred during the initial phase, a second phase of slow slips with higher slip rate (several hundreds of m/s) was often accompanied by the occurrence of small seismic events (foreshocks). We also found that the magnitude of foreshocks became larger under a higher local slip rate. These observations suggest that the asperities on the fault slip stably under the low local loading rate, but can slip rapidly and radiate seismic waves under the high local loading rate. Therefore, it is necessary to incorporate the effect of local loading rate into the studies of natural earthquakes.

1 Introduction

To predict when and where the next major earthquake will initiate is of great importance to both scientific research and disaster mitigation. It is well known that unstable fast rupture does not suddenly begin on a fault plane, but is often preceded by a quasi-stable slow slip, which is called the nucleation process. The transition from the slow slip to the fast rupture was first demonstrated by some pioneer laboratory experiments (Dieterich, 1978; Ohnaka & Kuwahara, 1990; Okubo & Dieterich, 1984). Ever since those earlier studies, more experimental studies have been conducted to improve the understanding of the nucleation process (e.g. Latour et al., 2013; McLaskey & Lockner, 2014; Nielsen et al., 2010; Ohnaka & Shen, 1999; Gvirtzman & Fineberg, 2021). In parallel, theoretical and numerical studies have also been conducted to investigate the nucleation process and to construct a comprehensive model for it (e.g. Ampuero & Rubin, 2008; Dieterich, 1992; Lapusta & Rice, 2003; Noda et al., 2013; Rubin & Ampuero, 2005; Uenishi & Rice, 2003).

The length of the slipping region, at which a stable slip transitions to an unstable rupture, is called the critical nucleation length h^*. Considering the conditions at the seismogenic depth, h^* and the associated slip amount expected from the above studies were supposed to be too small to be detected by observations at the Earth's surface. However, recent geodetic observations showed detectable crustal deformations preceding some large earthquakes (Ito et al., 2013; Ruiz et al., 2014, 2017; Socquet et al., 2017), though their behaviors are not so simple as the ones predicted by theoretical models.

Another possible way to detect the nucleation process is to monitor seismic activity, i.e., foreshocks. Although foreshocks do not always occur and are usually classified retrospectively, they can still provide us with valuable information for understanding the earthquake nucleation process. Several studies have reported foreshocks (Bouchon et al., 2013; Ruiz et al., 2017) and their migration (Kato et al., 2012; Ruiz et al., 2014) preceding some large earthquakes. Recent study also showed that even the nucleation process for a very small earthquake ($M3.7$) can be inferred from the detected foreshock activity, and further suggested that those foreshocks could be triggered by an underlying slow slip on the fault (Tape

et al., 2018). However, the exact triggering mechanism is still unknown.

Considering the complicated behaviors of earthquake nucleation process and the uncertainty of foreshock detection under a natural condition, laboratory experiment should be one of the best approaches for fully understanding those phenomena. Selvadurai and Glaser (2015) conducted direct shear experiments with PMMA blocks. They observed that high normal stress could suppress the propagation of slow slip and increase the foreshock size, which were reproduced by their numerical simulation. McLaskey and Lockner (2014) conducted friction experiment with saw-cut cylindrical granite samples using a triaxial loading apparatus. They observed accelerated seismic activity before each stick-slip event but found 98% of premonitory moment release was due to aseismic preslip. They proposed that the main stick-slip event was triggered by a cascade-up process assisted by the preslip. McLaskey and Kilgore (2013) observed foreshocks preceding stick-slip events on a 2-m long granite fault. Since the foreshocks only occurred at the final phase in the nucleation process, they proposed that the increased stressing rate during the nucleation caused a reduction of h^* and then triggered the foreshocks.

Recently, apparatuses for meter-scale rock friction experiments have been newly developed, which can provide more realistic conditions for investigating the earthquake nucleation process than the conventional small-scale experiments since the nucleation zone size can be within the sliding fault area. An apparatus using a large-scale shaking table has been developed and installed at the National Research Institute for Earth Science and Disaster Resilience (NIED) in Japan (Fukuyama et al., 2014). Large-scale friction experiments using this apparatus have been conducted, and effects of fault width (Fukuyama et al., 2018), fault roughness (Yamashita et al., 2018), and loading rate (Xu et al., 2018) on the rupture nucleation process were reported in detail. The research group also demonstrated that foreshocks, the locations of which coincided well with those of generated wear materials, were triggered right after the passage of a precursory slow slip front prior to the main rupture on a less heterogeneous fault (Yamashita et al., 2021). At Cornell University in the U.S., an apparatus that can shear 3-m long granite blocks has been developed. This apparatus successfully produced the initiation, propagation, and also termination of ruptures on the fault, which should be closer to natural earthquakes than the conventional stick-slip events (Ke et al., 2018). Using this apparatus, McLaskey (2019) proposed that the smooth nucleation process predicted by theory is hard to occur on natural rough faults, but foreshocks, which are produced during the nucleation process, finally trigger the main dynamic rupture.

In this paper, we also investigate the nucleation process of earthquakes in the laboratory, but with an even larger rock fault and much better instrumentations than previous studies. These advantages allow us to quantitatively understand the key factors that control the occurrence and magnitude of foreshocks during the experimentally simulated nucleation process. In the followings, we first introduce the basic experimental setup. Then, we show slow slip activity as

part of the nucleation process leading to the main event. Next, we compare the spatiotemporal distribution of foreshocks with that of local slip or local slip rate, and investigate the factors that control the occurrence and magnitude of foreshocks. Finally, we discuss the implications of the obtained results, and make the concluding remarks.

2 Method

2.1 Experimental setup

Figure 1a shows a schematic diagram of the newly developed apparatus for the current study. This apparatus enables us to shear 4-meter-long rock specimens. We used a pair of metagabbro blocks from India as the experimental specimen. The physical properties are listed in Table 1. The shorter block was stacked on the longer one as shown in Figure 1a. The nominal contacting area was 4.0 m long and 0.1 m wide, and is treated as the simulated fault in the current study. Normal load was applied with eight flat jacks installed side by side between the top frame of the apparatus and a steel plate on the top surface of the upper specimen. The dimension of a single flat jack was 0.5 m long and 0.1 m wide. The flat jacks were pressurized by the mixed fluid of oil and air in order to keep the pressure constant even if the flat jacks were deformed during an experiment. The pressure of the flat jacks was built up to an objective value before shearing and was maintained at a constant value by shutting each oil circuit off during an experiment. The pressure of each flat jack was separately monitored by a pressure gauge (GP-M100, Keyence Corp., Japan) to estimate the amount of normal stress on the simulated fault. According to a preliminary calibration by the manufacturer of the flat jack, the actual pressure applied by the flat jack is around 67% of its oil pressure, because the edges of the flat jack are not in contact with the pressurized face and thus the total contacting area is inevitably smaller than the whole fault area. To retrieve the actual pressure value, we first averaged the oil pressures over eight flat jacks and then reduced the averaged value to 67%. We treated the obtained value after the 33% reduction as the macroscopic normal stress ( ) on the simulated fault. Shear load was applied by a hydraulic jack installed at the western end of the apparatus. The western end of the lower specimen was loaded by this jack. The lower specimen was put on a low-friction roller on the bottom frame, so that only the simulated fault supported the shear load. The amount of shear load was measured with a load cell (CLP-2MNS006, Tokyo Measuring Instruments Laboratory Co., Ltd., Japan) installed between the hydraulic jack and the lower specimen. Therefore, the amount of macroscopic shear stress ( ) was obtained from the measured shear load divided by the fault area.

Table 1 *Properties of rock specimen*

Item	Property
Rock type	Metagabbro
Dimension for upper specimen	L4.0 m x W0.1 m x H0.2 m

Item	Property
Dimension for lower specimen	L4.1 m x W0.1 m x H0.2 m
Nominal dimension of contacting area	L4.0 m x W0.1 m
Initial undulation of contacting surface	< 10 m
Young's modulus	103 GPa
Poisson's ratio	0.31
P-wave velocity*	6919 m/s
S-wave velocity*	3631 m/s

*Seismic wave velocities were estimated from Young's modulus, Poisson's ratio, and density.

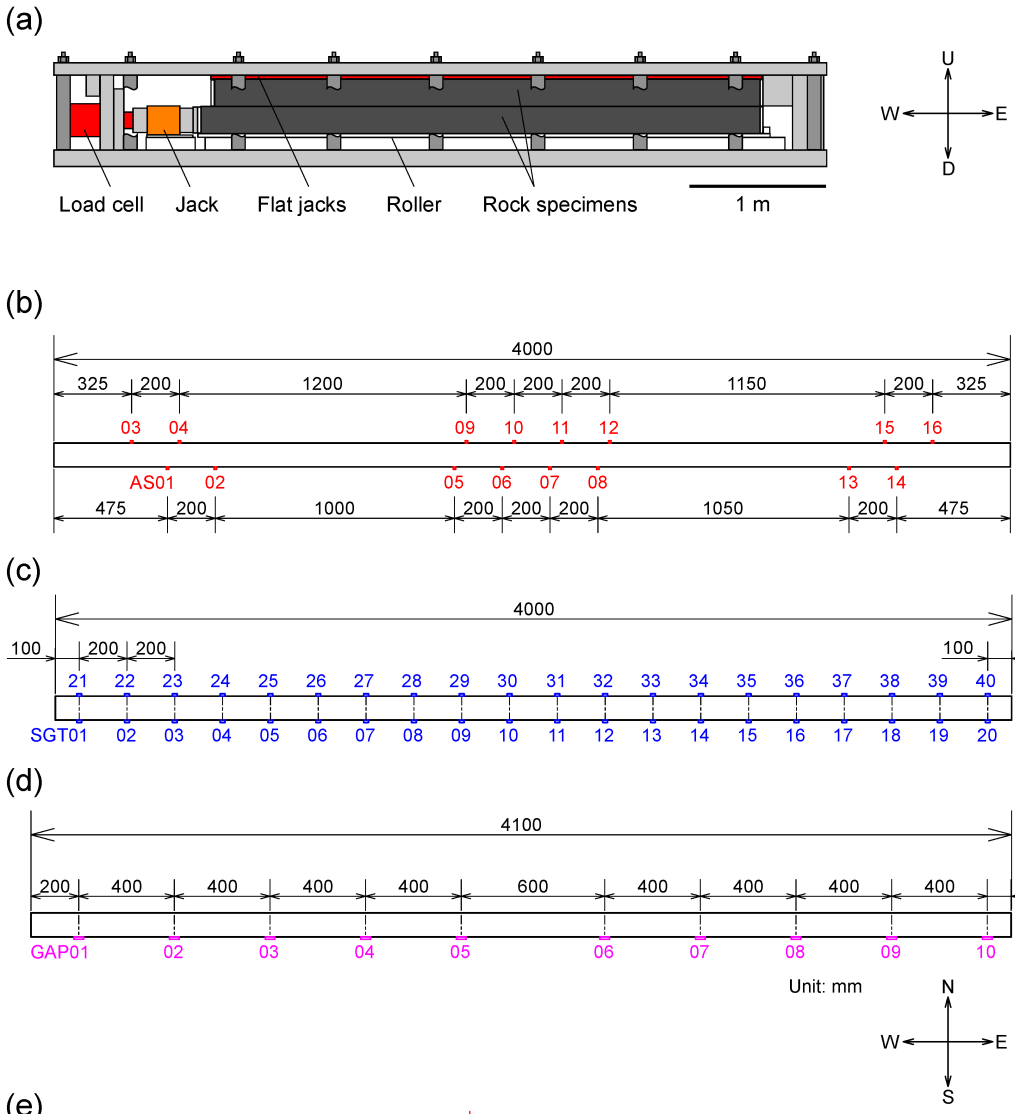
(a)
Load cell
Jack
Flat jacks
Roller
Rock specimens
1 m
U
W
E
D
(b)
4000
325
200
1200
200
200
200
1150
200
325
03
04
09
10
11
12
15
16
AS01
02
05
06
07
08
13
14
475
200
1000
200
200
200
1050
200
475
(c)
4000
100
200
200
100
21
22
23
24
25
26
27
28
29
30
31
32
33
34
35
36
37
38
39
40
SGT01
02
03
04
05
06
07
08
09
10
11
12
13
14
15
16
17
18
19
20
(d)
4100
200
400
400
400
400
600
400
400
400
400
100
GAP01
02
03
04
05
06
07
08
09
10
Unit: mm
N
W
E
S
(e)
AS
70
15
15
SGT
GAP
10
4
Target
Probe holder
Unit: mm
U
W
E
D
for AS, GAP, and SGT01 to SGT20
U
E
W
D
for AS and SGT21 to SGT40

Figure 1. Experimental setup in this study. (a) Schematic diagram of rock friction apparatus at NIED. An upper rock specimen is vertically stacked on a lower rock specimen. Normal load is applied by eight flat jacks inserted side by side between upper frame of the apparatus and the upper specimen. Oil pressures of the flat jacks are maintained at a constant value by closing the oil circuit during an experiment. Shear load is applied by laterally pushing the lower specimen with a hydraulic jack. The amount of normal stress ( ) on the simulated fault is assumed to be 67% of the averaged oil pressure of eight flat jacks. The amount of shear stress ( ) is estimated from the amount of load measured with a load cell. Map view of the upper specimen indicating the locations of (b) 16 acoustic sensors (AS) and (c) 40 triaxial semiconductor strain gauges (SGT). (d) Map view of the lower specimen indicating the location of 10 eddy current gap sensors (GAP). (e) Side view showing the configurations of various sensors. The target of GAP is installed on the side surface of the upper specimen.

We repeated the experiments with the same pair of rock specimens (named FB02) under the same normal stress around 4 MPa. Because we manually pumped up the hydraulic jack to apply the shear load in the experiments, the loading rate was not well controlled. Nevertheless, we tried to keep the shear loading rate as uniform as possible, but also with fast or slow rates in order to investigate the influence of macroscopic loading rate on the fault rupture process. In the current study, we investigate two experiments FB02-006 and FB02-008 with relatively high shear loading rate, as well as two other experiments FB02-007 and FB02-010 with relatively low loading rate. See Table 2 for the actual loading rate in each experiment. Because of the effective range of eddy current gap sensor described in the next section, the total amount of displacement during a single experiment was limited within 2 mm. Five experiments have been done before FB02-006. It is supposed that some amount of wear materials was produced on the fault. The wear materials were kept on site throughout all the experiments.

Table 2 *Macroscopic shear loading rate and local slip rate during long-term slow slip*

Experiment ID	Macroscopic shear loading rate (kPa/s)	Slip rate at GAP01 during long-term slow slip (µm/s)
FB02-006	±15.5	±3.4
FB02-007	±1.7	±0.3
FB02-008	±28.5	±9.5
FB02-010	±1.5	±0.6

2.2 Measurements

Signal from the load cell was processed with a strain amplifier (CDV-71A, Kyowa Electronic Instruments Co., Ltd., Japan). The oil pressure of the pressure gauge for the flat jack was output as electrical signals. Those signals were continuously sampled at 1 MHz with 16-bit resolution (M2i4741-mgt, Spectrum Instrumentation, Germany). In addition to the macroscopic monitoring, we installed 16 broadband acoustic sensors (V103-RM, Olympus Corp., Japan) named AS, 40 triaxial semiconductor strain gauges (SKS-30282, Kyowa Electronic Instruments Co., Ltd., Japan) named SGT, and 10 eddy current gap sensors (FK-202F, Shinkawa Electric Co., Ltd., Japan) named GAP along the fault, in order to monitor the local phenomena on the fault in detail (Figures 1b-1e). ASs were installed on both side surfaces of the upper specimen, 70 mm away from the simulated fault (Figures 1b and 1e). AS has a resonance frequency at 1 MHz and the signal was amplified 20 times by a custom-made amplifier (Turtle Industry Co., Ltd., Japan). The amplified signal was continuously sampled at 10 MHz with 14-bit resolution (M2i4032, Spectrum Instrumentation, Germany). SGTs were installed on both side surfaces of the upper specimen, 10 mm away from the simulated fault (Figures 1c and 1e). Three strain gauge components were offset by 45, 90, and 135 degrees from the horizontal fault plane as shown in Figure 1e. The strain signal from each component was individually processed with a signal conditioner (CDA-700A or CDA-900A, Kyowa Electronic Instruments Co., Ltd., Japan) and continuously sampled at 1 MHz with 16-bit resolution (M2i4741-mgt, Spectrum Instrumentation, Germany or PXIe-6358, National Instruments Corp., USA). GAP can measure the relative horizontal displacement between the edge of a probe and a steel target. The probe was fixed by an aluminum holder glued on the side surface of the lower specimen. The steel target was glued on the side surface of the upper specimen (Figure 1e). This transducer has a flat sensitivity up to 10 kHz, and the signal was continuously sampled at 50 kHz with 24-bit resolution (LX-120, TEAC Corp., Japan). The measurement range of GAP was from 0.25 mm to 2 mm.

3 Basic results

In every experiment, stick-slip events were observed, which is consistent with the velocity-weakening behavior of metagabbro in the framework of the rate- and state-dependent friction (RSF) law reported by a previous study (Urata et al., 2017). In order to compare the results of the four experiments under a similar condition, we picked up the last seven stick-slip events right before the total amount of slip reached 2 mm and then named those events evt-1 to evt-7. Figures 2a, 2d, 2g, and 2j show the evolution of macroscopic / for the last seven events. The macroscopic loading rate shown in Table 2 was obtained from the averaged trends during the shear loading stage before each stick-slip event.

Seismic signals associated with the stick-slip events are presented in Figures 2b, 2e, 2h, and 2k. Those panels show the sum of squared amplitude over all AS channels (on a logarithmic scale) during a 0.1 ms time interval. High value of the sum means a large seismic energy release at the time. Colored cross

symbols represent detected repeating seismic events, which will be explained in Section 4.4. We detected local peaks of the calculated sum and then picked up a time-window like the one in Figure 3. Figures 3a and 3b show the records of AS and those of shear stress (converted from SGT) over the same time period, respectively. As seen, a small seismic event (sevt) was clearly captured by both the AS array (Figure 3a) and the SGT array (Figure 3b).

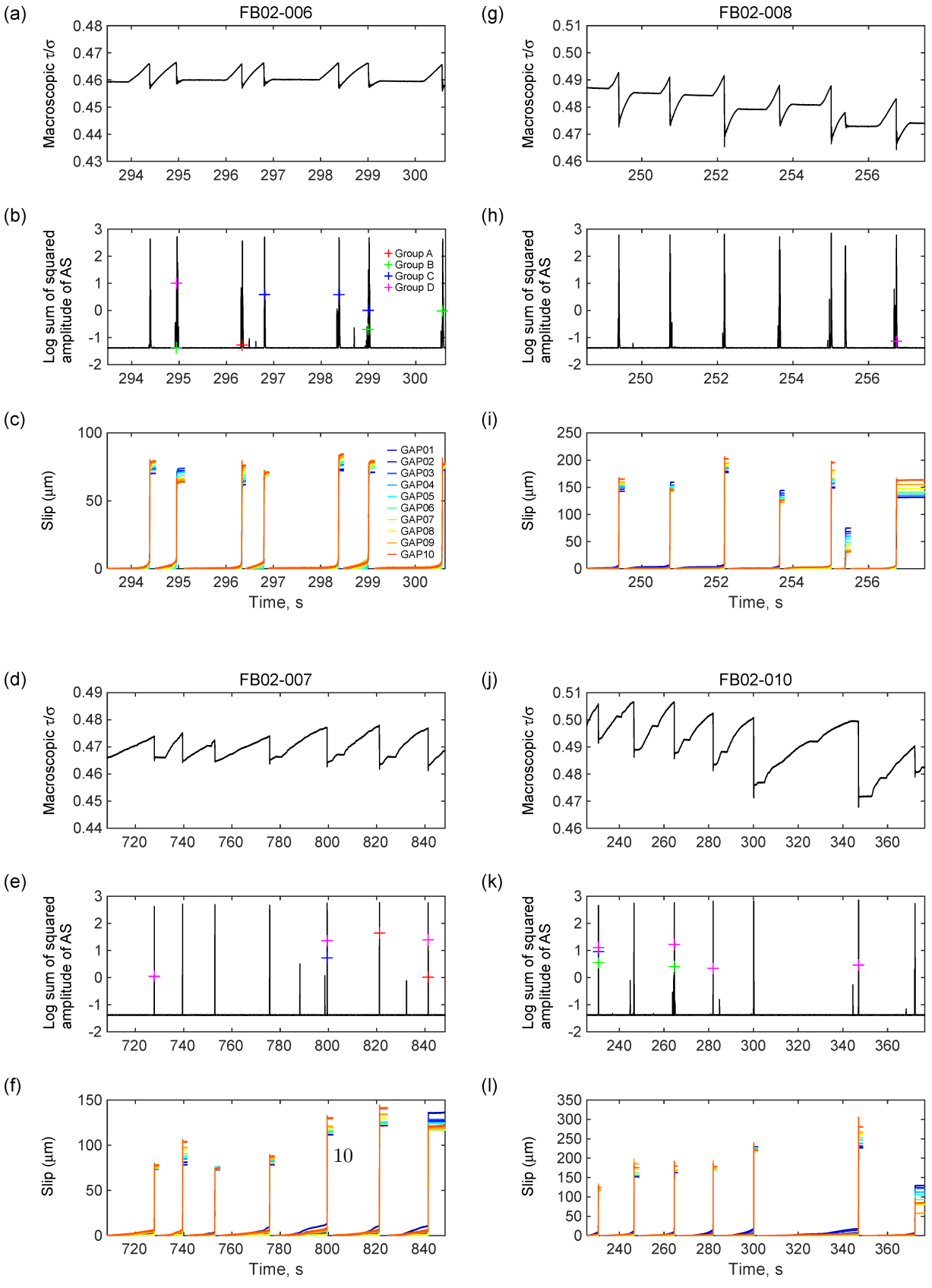
(a)
FB02-006
Macroscopic τ/σ
0.48
0.47
0.46
0.45
0.44
0.43
294 295 296 297 298 299 300
(b)
Log sum of squared amplitude of AS
3 2 1 0 -1 -2
Group A
Group B
Group C
Group D
294 295 296 297 298 299 300
(c)
Slip (μm)
100 50 0
GAP01
GAP02
GAP03
GAP04
GAP05
GAP06
GAP07
GAP08
GAP09
GAP10
294 295 296 297 298 299 300
Time, s
(g)
FB02-008
Macroscopic τ/σ
0.51 0.50 0.49 0.48 0.47 0.46
250 252 254 256
(h)
Log sum of squared amplitude of AS
3 2 1 0 -1 -2
250 252 254 256
(i)
Slip (μm)
250 200 150 100 50 0
250 252 254 256
Time, s
(d)
FB02-007
Macroscopic τ/σ
0.49 0.48 0.47 0.46 0.45 0.44
720 740 760 780 800 820 840
(e)
Log sum of squared amplitude of AS
3 2 1 0 -1 -2
720 740 760 780 800 820 840
(f)
Slip (μm)
150 100 50 0
720 740 760 780 800 820 840
Time, s
(j)
FB02-010
Macroscopic τ/σ
0.51 0.50 0.49 0.48 0.47 0.46
240 260 280 300 320 340 360
(k)
Log sum of squared amplitude of AS
3 2 1 0 -1 -2
240 260 280 300 320 340 360
(l)
Slip (μm)
350 300 250 200 150 100 50 0
240 260 280 300 320 340 360
Time, s

Figure 2. (a) Macroscopic / , (b) logarithmic sum of squared amplitude of AS output, and (c) amount of slip for experiment FB02-006. (d)-(f) Similar to (a)-(c) but for experiment FB02-007. (g)-(i) Similar to (a)-(c) but for experiment FB02-008. (j)-(l) Similar to (a)-(c) but for experiment FB02-010. Cross symbols in (b), (e), (h), and (k) indicate the occurrence time of repeating foreshocks (see section 4.4). The amount of slip at each channel in (c), (f), (i), and (l) is reset to zero after each main stick-slip event.

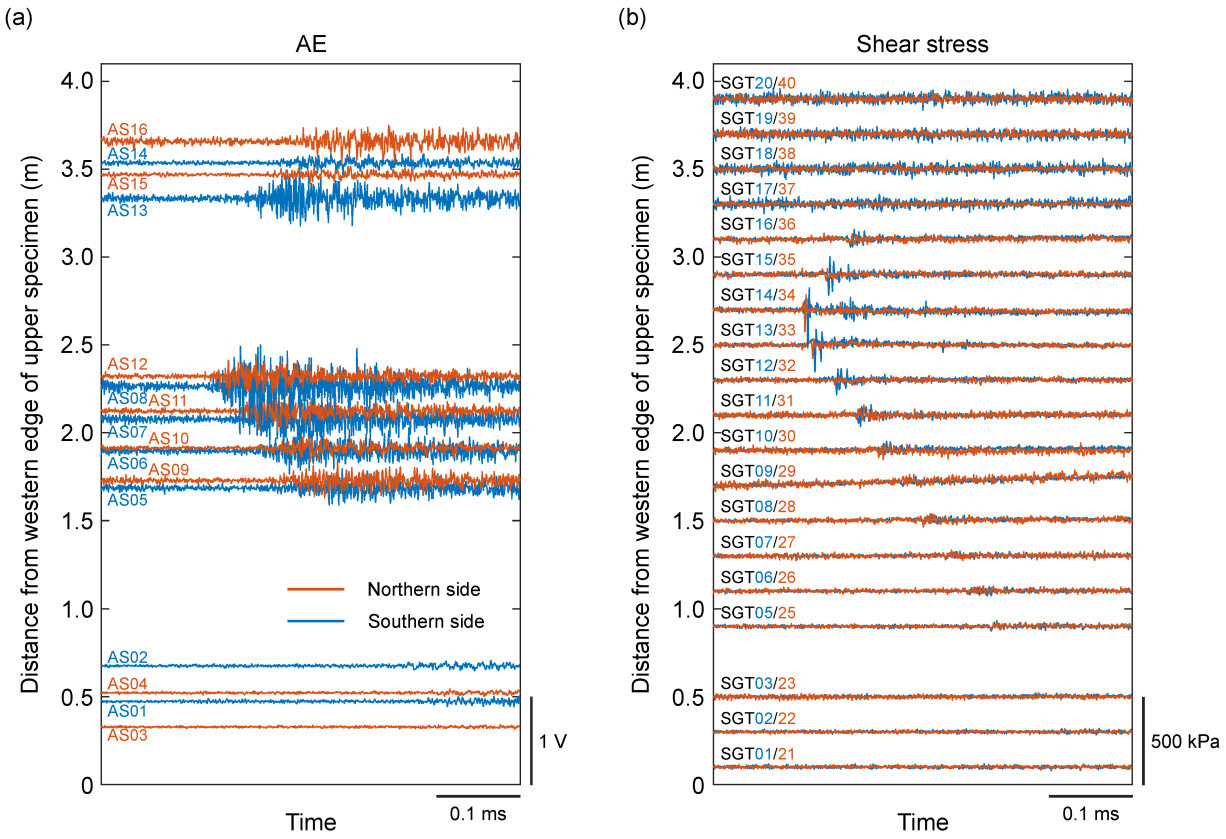

Figure 3. Typical foreshock waveforms observed by (a) the acoustic sensor AS array and (b) the strain gauge SGT array over the same time period. The waveform in (b) shows shear stress along the fault, which was calculated from the measured strain. Data of SGT04 and SGT24 are not displayed because of their abnormal values caused by a local crack in the rock specimen. The label at the left end of each waveform indicates the location of the associated sensor.

Figures 2c, 2f, 2i, and 2l show the fault slips between and during the stick-slip events. Note that the amount of slip was reset to zero after every stick-slip event in these panels. The total amount of slip over a single stick-slip cycle was around 100 m on average. It should be noted that the slips at both the leading and

trailing edges were gradually increasing even at the shear loading stage, which is more significant in the experiments with low loading rate (FB02-007 and FB02-010). Figure 4a shows the detailed spatiotemporal distribution of slip along the fault in a stick-slip cycle, where dense and sparse contour lines represent slow and fast slip during different stages of the stick-slip event, respectively. Figure 4b shows the early-stage evolution of local fault slip before the main slip event, which clearly reveals that both the leading and trailing edges began to slip at first and kept slipping for a long time; we call this slip behavior "long-term slow slip" in this study. Comparison between the macroscopic loading rate and the local slip rate suggests that this long-term slow slip is dominantly controlled by the macroscopic shear loading (see Table 2 and Appendix A.2). The slipped areas gradually enlarged toward the central area of the fault, and then fast slip was initiated after the two slipped areas coalesced at the along-fault location of ~ 1.7 m. Figure 4c shows the slip evolution after the coalescence, which is called "precursory slow slip" in this study. We will discuss why and how the long-term slow slip was generated in section 4.1, and will examine the relation between seismic activity and local slip activity in sections 4.2, 4.3 and 4.4.

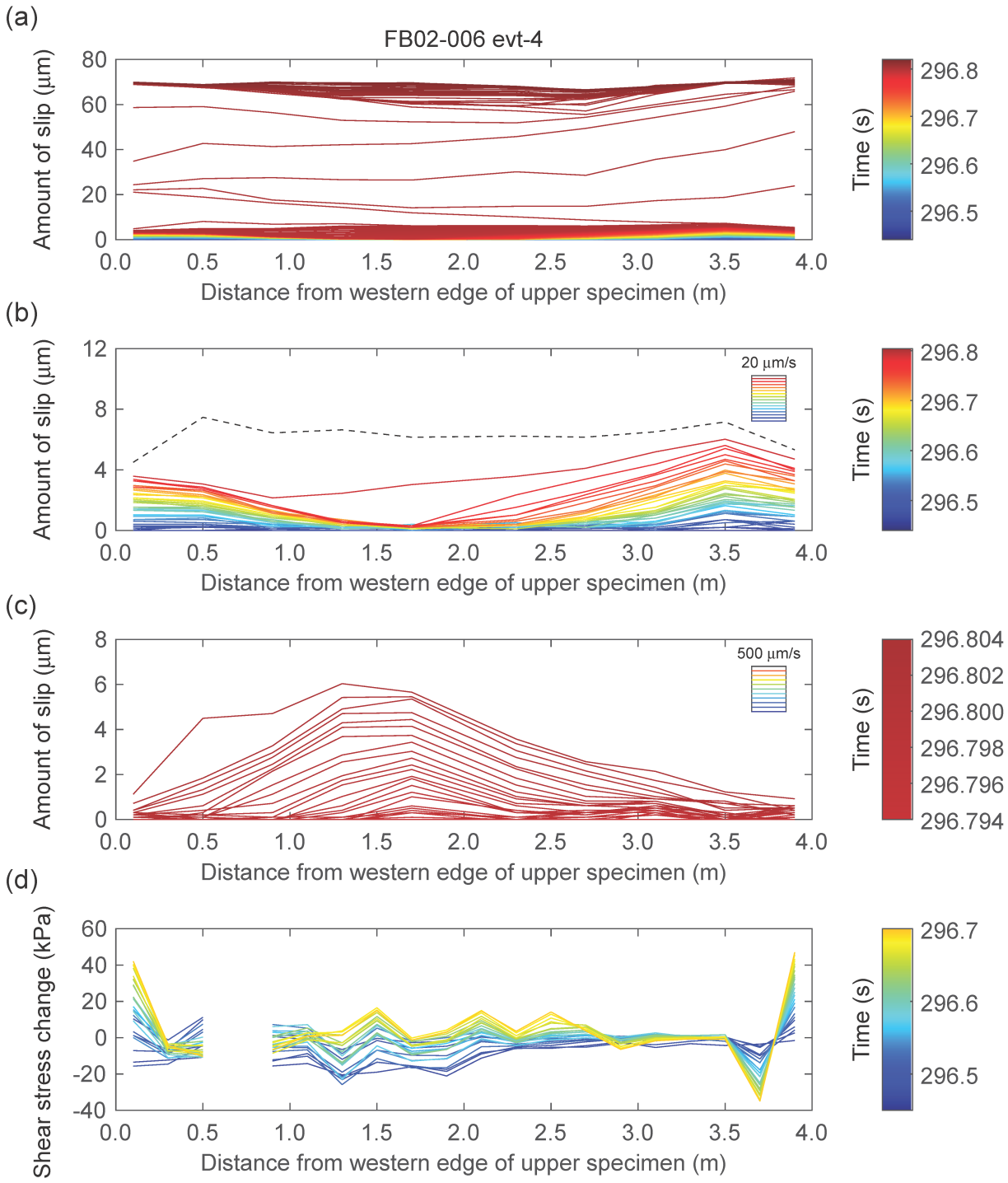
(a)
FB02-006 evt-4
Amount of slip (μm)
Distance from western edge of upper specimen (m)
Time (s)
(b)
20 μm/s
(c)
500 μm/s
(d)
Shear stress change (kPa)

Figure 4. (a) Spatiotemporal evolution of slip along the fault for a stick-slip event evt-4 in FB02-006. Contour lines are drawn every 0.4 ms. The amount of local slip was reset to zero after the previous event evt-3. (b) Enlarged view of the amount of local slip until the initiation of the main fast slip. Contour lines are drawn every 10 ms. Black dashed line indicates the amount of slip at the moment when the main fast slip initiated (see Appendix A.1 for the procedure of detecting the moment). (c) Slip evolution during the last 10 ms time window right before the initiation of the main fast slip. The amount of local slip was reset to zero at the beginning of this 10 ms time window. Contour lines are drawn every 0.4 ms. (d) Change in the local shear stress from 296.45 s to 296.70 s estimated from the northern strain gauge array (SGT21 - SGT40). The amount of shear stress was reset to zero at the beginning of this time window. Contour lines are drawn every 10 ms. The data of SGT24, which was installed at 0.7 m from the western edge, was removed from this plot because of its abnormal value caused by a local crack in the rock specimen. Colors of contour lines indicate time, and the indexes are common among (a), (b), (c), and (d).

4 Detailed analyses

4.1 Long-term slow slip

In order to understand why the long-term slow slip initiated from both edges of the fault (Figure 4b), we conducted a finite element method (FEM) modeling. We used a FEM program, Salome-Meca produced by EDF (Électricité de France, http://www.code-aster.org). This program composed of a pre- and post-processor SALOME and a solver Code_Aster. Figures 5a-c show a model constructed for the FEM calculation. This model consisted of vertically stacked rock blocks and a steel plate on the upper rock block, whose dimensions were the same as those for real specimens and part of the apparatus in the current experiments. Note that only the southern half of the system was modeled because of the symmetry in the north-south direction. Young's modulus and Poisson's ratio for the steel plate were 200 GPa and 0.30, respectively, and those for the rock blocks were shown in Table 1. The contacting interfaces between the upper and the lower rock blocks had a static friction coefficient of 0.75. We divided this model into 357,783 elements, the shape of which was tetrahedron except for regions around the contacting interfaces. In order to make rectangular mesh on the interfaces, quadrangular-pyramid-shaped elements were arranged there. The maximum mesh size was 25 mm and that on the contacting interfaces was 5 mm. Because of the symmetry, a fixed boundary condition was applied to the northern side face of the model in the north-south direction (Figure 5b). At the top, 6-MPa-pressure was applied at eight rectangular regions on the steel plate, to simulate the normal load from the eight flat jacks to the fault (Figure 5c). The bottom face of the lower rock block was fixed in the up-down direction (Figure 5c). The eastern side face of the upper rock block was also fixed in the east-west direction (Figures 5b and 5c). After applying the normal load, we gradually increased the shear load to the western side face of the lower rock block (Figures 5b and 5c).

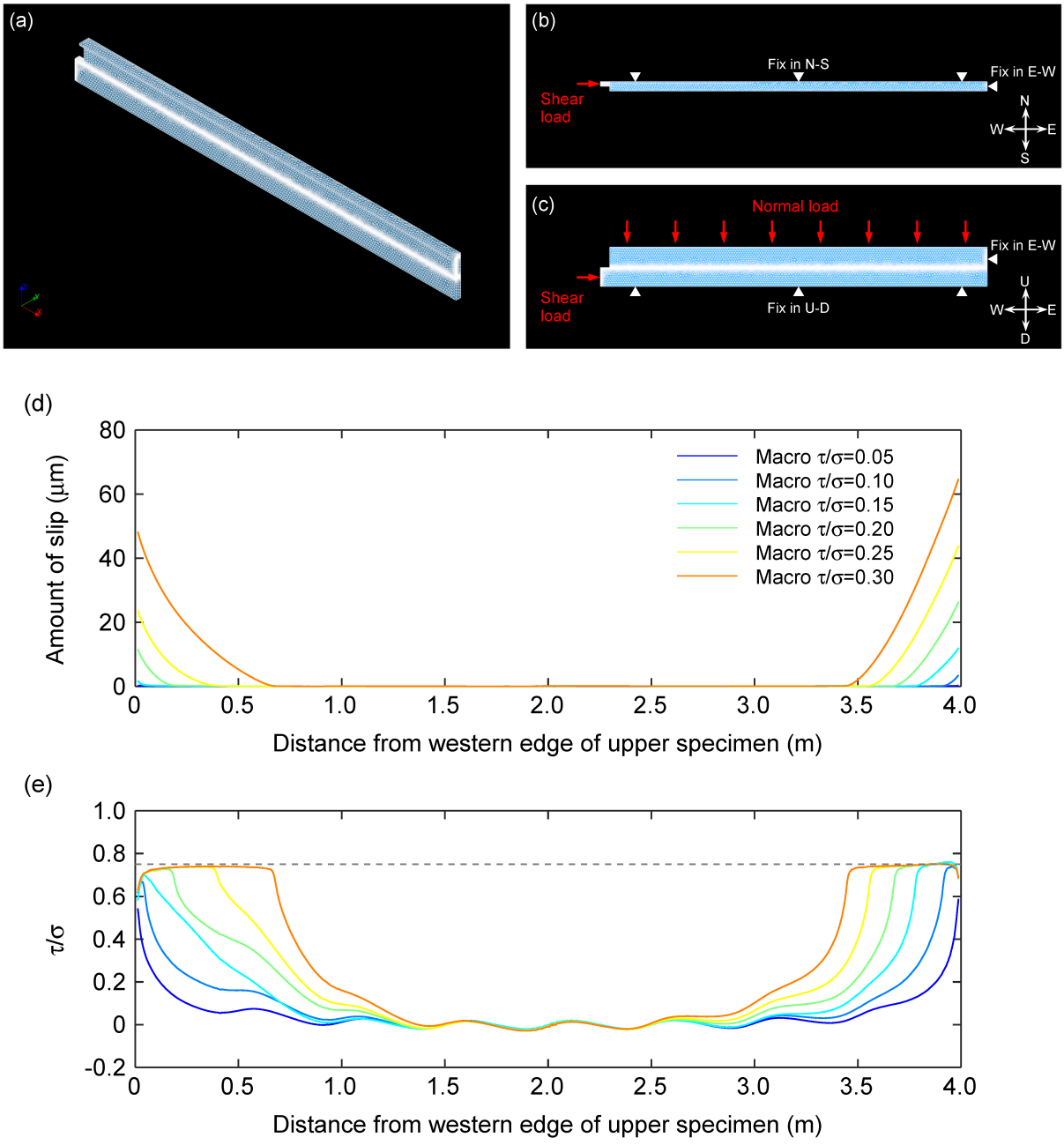

Figure 5. Configuration of FEM calculation for the current experimental setup and the results. View of the mesh model from (a) diagonally above, (b) top, and (c) south. Only the southern half was modeled because of symmetry. Evo-

lutions of (d) the local slip and (e) the local / distribution with increasing the macroscopic shear stress obtained from the FEM calculation. Dashed line in (e) represents / of 0.75, which is the static friction coefficient of the contacting interfaces defined in the FEM calculation. Features of the slip initiations and the increase in shear stress from both edges of the fault are consistent with the observations shown in Figures 4b and 4d, respectively.

The calculated evolutions of local slip and / are shown in Figures 5d and 5e, which simulated the situations when the macroscopic / increased from 0.05 to 0.30. Note that displayed slip and / were averaged values along the north-south axis. As shown in Figure 5e, the local / increased and attained the assumed static friction coefficient at both edges, which led to the local fault slips as shown in Figure 5d. With increasing the applied shear load and thus macroscopic / , the slipped area expanded toward the central locked area from both edges, which is similar to the observed behavior shown in Figure 4b. We also note that the calculated evolution of / (Figure 5e) is also similar to the observed shear stress evolution (Figure 4d).

4.2 Foreshock activity and accumulated slip

The occurrence times of seismic events, as roughly estimated from the AS amplitude (Figures 2b, 2e, 2h, and 2k), suggest that most of the small seismic events occurred right before the main stick-slip events (see Figure B1 for a close-up view of FB02-006 evt-1). Therefore, they can basically be categorized as "foreshocks". We defined the seismic events that occurred in the second half of recurrence time since the previous stick-slip event as foreshocks and then focused on their activities in the current study. Based on the seismic record, we determined the origin time and hypocenter location of the foreshocks (See Appendix B.1 for the procedure). Figure 6 shows the located hypocenters of the foreshocks. The numbers of located foreshocks for FB02-006, FB02-007, FB02-008, and FB02-010 are 47, 28, 32, and 54, respectively, which suggests that foreshock activity is not directly relevant to the macroscopic loading rate (Table 2) in the current experiments.

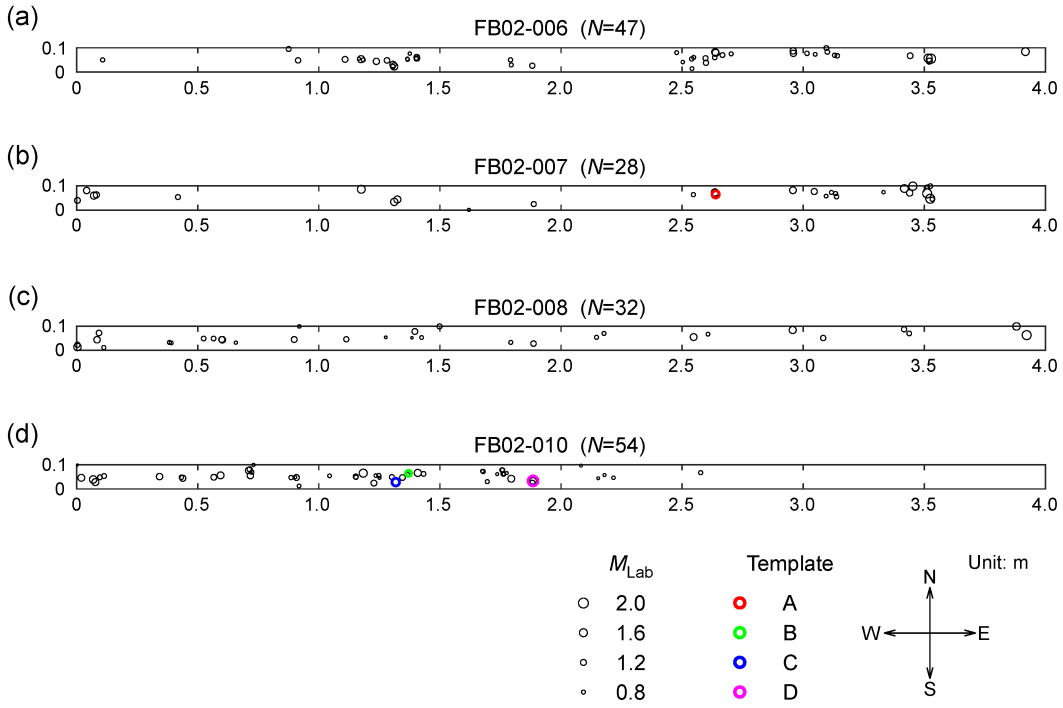

Figure 6. Hypocenters of foreshocks for (a) FB02-006, (b) FB02-007, (c) FB02-008, and (d) FB02-010. The size of circles scales with the laboratory-specific magnitude (M_{Lab}) of foreshocks. The colored circles indicate the hypocenters of template foreshocks (see section 4.4).

Based on the foreshock catalog, we investigated the relationship between foreshock activity and local slip activity. Figure 7a compares spatiotemporal distribution of the foreshocks with that of the local slip right before a main stick-slip event (evt-5) in the experiment with low loading rate (FB02-007). Note that the shown result represents the amount of slip accumulated after the previous main stick-slip event (evt-4). There exists a significant variation in the accumulated slip along the fault: the accumulated slip reached more than 10 µm at the western edge whereas it was almost zero at the central area. Figure 7a also shows that foreshocks occurred right before the main stick-slip event (black dashed line), regardless of the amount of accumulated slip there. This situation is common among other events including the case with high loading rate, for example FB02-008, as shown in Figure 7b.

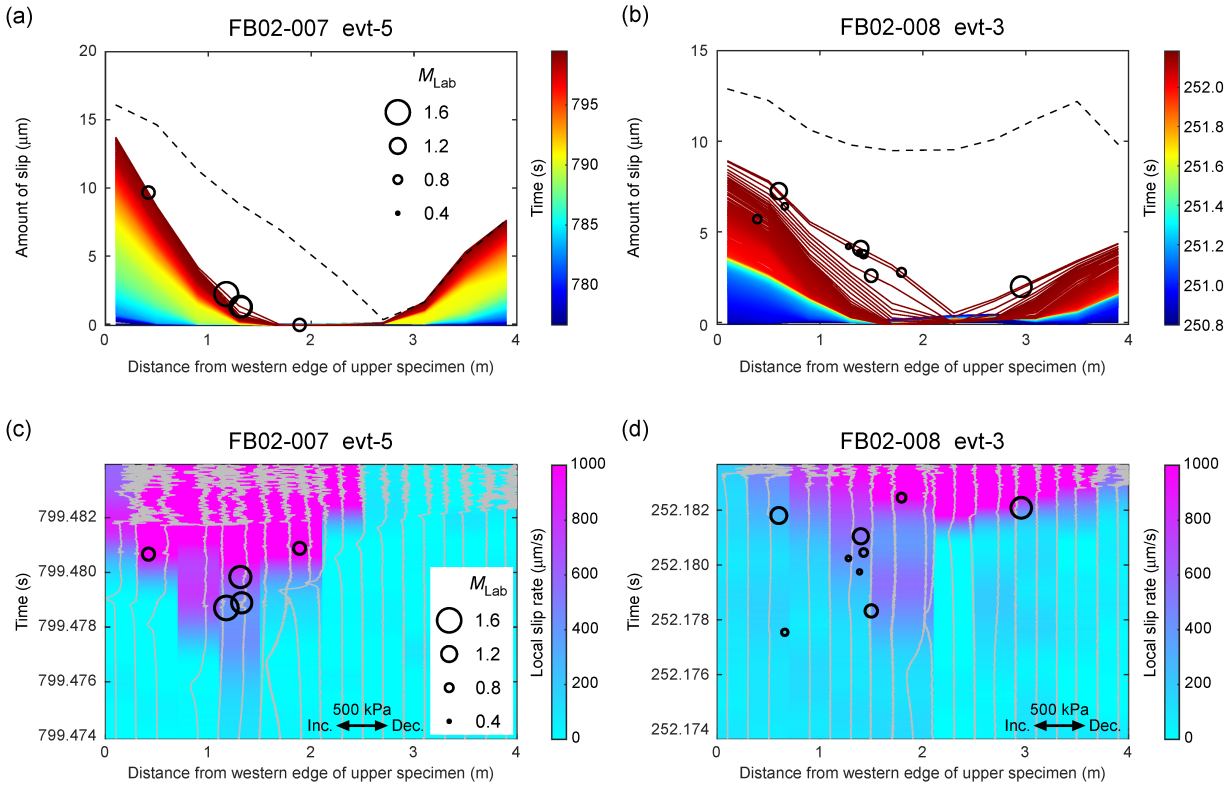

Figure 7. Comparison between spatiotemporal distribution of the foreshocks and that of the slip accumulated after the previous stick-slip event right before the initiation of the main fast slip for (a) evt-5 in FB02-007 and (b) evt-3 in FB02-008. Contour lines are dawn every 20 ms for (a) and 2 ms for (b). Black dashed line indicates the amount of slip at the moment when the main fast slip initiated. The amount of accumulated slip shows no clear correlation with the occurrence of the foreshocks. Comparison between spatiotemporal distribution of the foreshocks and that of the slip rate during a 10 ms time window right before the initiation of the main fast slip for (c) evt-5 in FB02-007 and (d) evt-3 in FB02-008. Gray lines show changes in shear stress estimated from the northern strain gauge array (SGT21 - SGT40). Bottom end of each gray line indicates the location where the associated strain gauge was installed. Foreshocks occurred when the local slip rate reached at several hundreds of μm/s.

4.3 Foreshock activity and local slip rate

Next we compared the spatiotemporal distribution of the foreshocks with that of the local slip rate. To obtain the slip rate, we calculated the time derivative of slip measured by each GAP sensor. Color map in Figure 7c shows the distri-

bution of the calculated slip rate. Note that the slip data were smoothed with splines before the calculation of time derivative just for clear view in this figure. Gray lines show changes in shear stress estimated from the northern SGT array (SGT21-SGT40). The strain data show temporal increase and subsequent decrease in the shear stress and its outward propagation from the central area, which should represent a nucleation process. An example for the slip evolution during the nucleation process (called precursory slow slip) is already shown in Figure 4c, which is a common feature among the nucleation processes of many other events. The local slip rate increased with the progression of the nucleation process, and then the foreshocks occurred when the local slip rate reached at several hundreds of µm/s. This situation is also common for the experiment with high loading rate (Figure 7d).

In order to quantify the relationship between foreshock occurrence and local slip rate, we estimated the local slip rate around the site of foreshock hypocenter, $\dot{D}_{\mathrm{loc}}$ (See Appendix A.3 and Figure A3 for the estimation), which was obtained by spatial interpolation. Figure 8 shows a histogram of foreshocks as a function of the estimated $\dot{D}_{\mathrm{loc}}$. As clearly demonstrated, the number of foreshocks is significantly high between 100 µm/s and 1000 µm/s of $\dot{D}_{\mathrm{loc}}$.

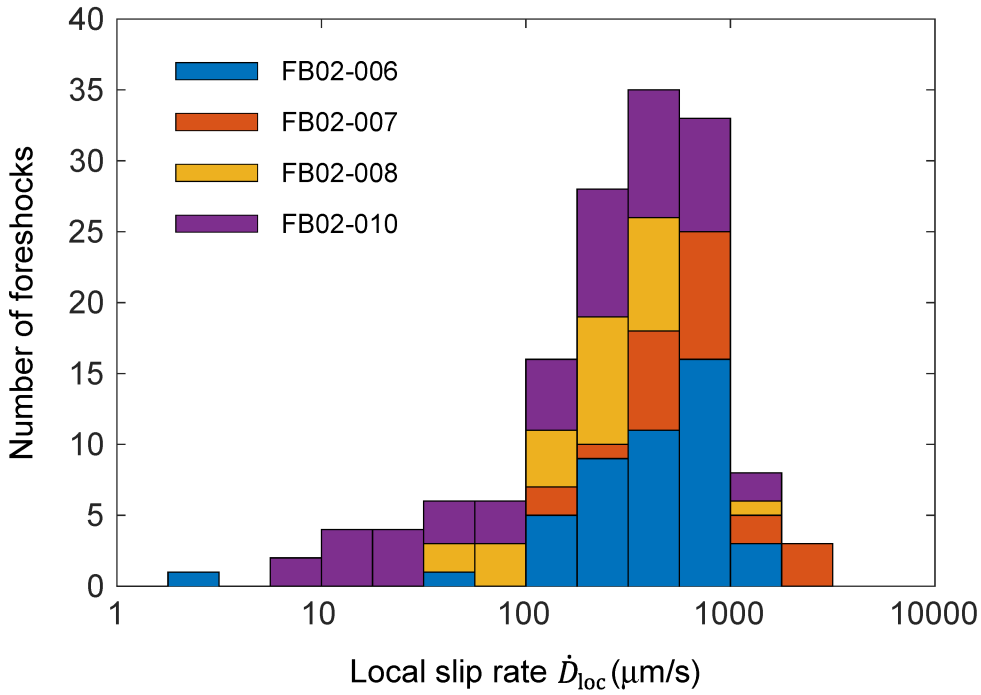

Figure 8. Histogram of foreshocks as a function of local slip rate $\dot{D}_{\mathrm{loc}}$ estimated at the same site and time. The number of foreshocks increases rapidly when $\dot{D}_{\mathrm{loc}}$ exceeds 100 m/s.

4.4 Foreshock magnitude and local slip rate

We next investigated the relationship between foreshock magnitude and local slip rate. We first simply compared a laboratory-specific magnitude M_{Lab} (See Appendix B.1) with $\dot{D}_{\mathrm{loc}}$, which resulted in a weak positive correlation between them as shown in Figure 9a (correlation coefficient between common logarithm of $\dot{D}_{\mathrm{loc}}$ and M_{Lab} equals 0.22). Here, it should be noted that this comparison was performed over all the foreshocks, at different locations, with various magnitudes, and under different loading conditions. In order to focus on the specific role of local slip rate and to exclude other effects, we searched for foreshocks that repeatedly occurred at the same location over four experiments by adopting the matched filter technique (MFT; See Appendix B.2 for the procedure). MFT has been widely used for detecting various seismic events such as low-frequency earthquakes (Shelly et al., 2007), aftershocks (Peng & Zhao, 2009), and foreshocks (Kato et al., 2012). Here we assume that the status of each location that could host repeating foreshocks was stable throughout the four experiments. As the result of MFT, we identified four groups of repeating foreshocks (See Figures 2b, 2e, 2h, 2k, 6, and Table B1). We then compare the magnitude of the repeating foreshocks with $\dot{D}_{\mathrm{loc}}$.

For the foreshock magnitude, we have already obtained M_{Lab} as a laboratory-specific magnitude. However, it should be noted that the estimation might not be precise enough for capturing a subtle variation in the magnitude of the repeating foreshocks. For example, error in the hypocenter location can affect the estimation because the distance between the hypocenter and the station is included in its calculation as shown in eq. (B.4). Therefore, for more robust comparison, we estimated the relative magnitude of the foreshock M_{r} based on the amplitude ratio of the waveforms (see Appendix B.3 for the procedure). Figures 9b-e compare the estimated M_{r} with $\dot{D}_{\mathrm{loc}}$. Those figures show a clear positive correlation between them except for Group B (correlation coefficients between common logarithm of $\dot{D}_{\mathrm{loc}}$ and M_{r} for Group A, B, C, and D are 1.00, -0.44, 0.72, and 0.50, respectively).

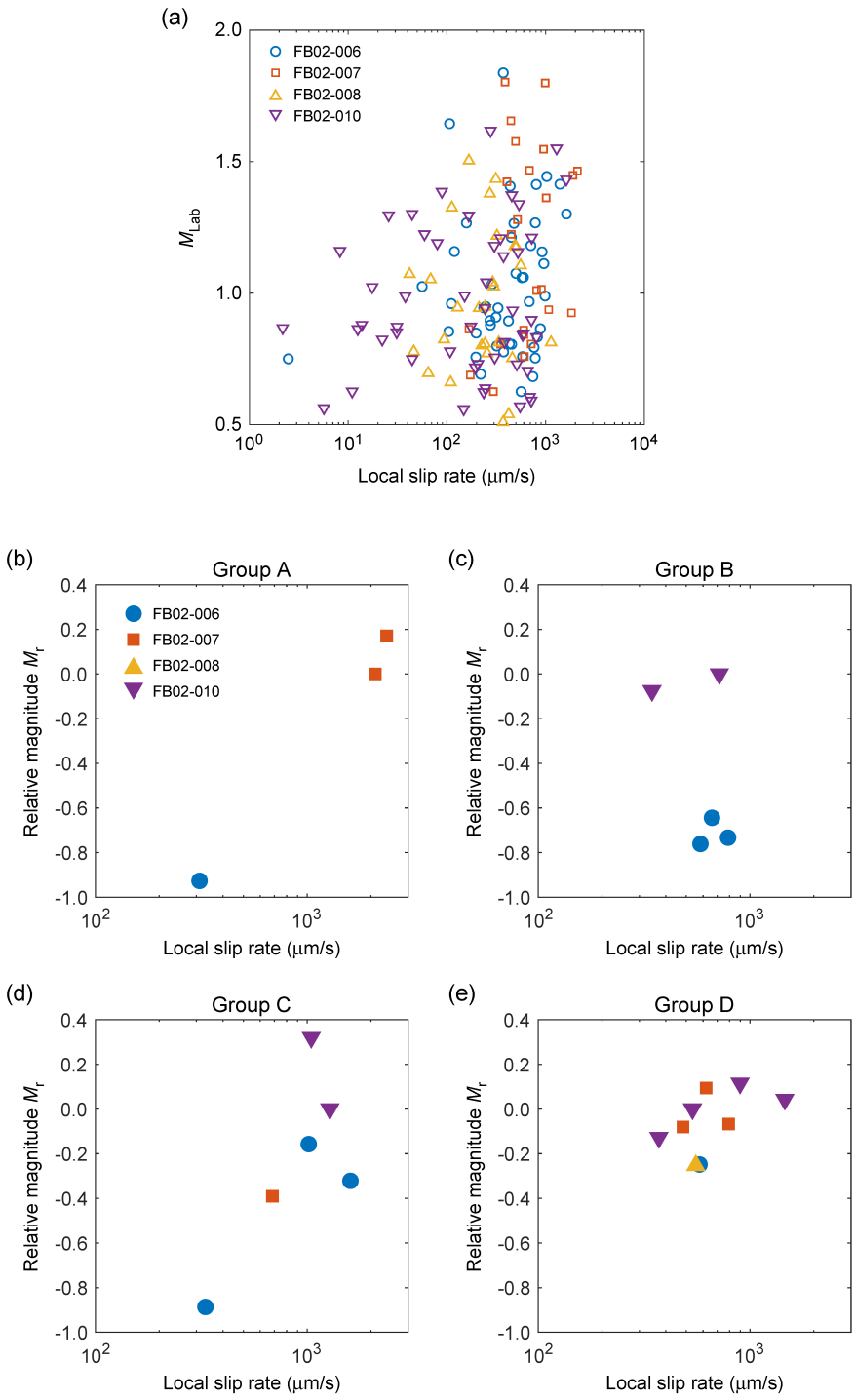
(a)
FB02-006
FB02-007
FB02-008
FB02-010
M_{Lab}
Local slip rate (μm/s)
(b)
Group A
Relative magnitude M_r
Local slip rate (μm/s)
(c)
Group B
Relative magnitude M_r
Local slip rate (μm/s)
(d)
Group C
Relative magnitude M_r
Local slip rate (μm/s)
(e)
Group D
Relative magnitude M_r
Local slip rate (μm/s)

Figure 9. (a) Comparison between the local slip rate $\dot{D}_{\mathrm{loc}}$ and the laboratory-specific magnitude M_{Lab}. Correlation coefficient between common logarithm of $\dot{D}_{\mathrm{loc}}$ and M_{Lab} is 0.22. Comparison between the local slip rate $\dot{D}_{\mathrm{loc}}$ and the relative magnitude M_{r} for (b) Group A, (c) Group B, (d) Group C, and (e) Group D. Correlation coefficients between common logarithm of $\dot{D}_{\mathrm{loc}}$ and M_{r} for Group A, B, C, and D are 1.00, -0.44, 0.72, and 0.50, respectively.

5 Discussion

5.1 The cause of long-term slow slip and its characteristics

We have conducted rock friction experiments using the newly developed apparatus. The most distinctive feature of this apparatus is that it can shear 4-m-long rock specimens, which could cause unique phenomena such as the long-term slow slip shown in Figure 4b. We observed that the long-term slow slip individually initiated from both the leading and trailing edges of the fault and the slipped areas gradually expanded toward the central fault area before most of the main stick-slip events. This behavior is quite consistent with the results of the FEM calculation as shown in Figures 5d and 5e. It is well known that local normal and shear stresses can concentrate at around edges of a laboratory fault by the edge effect (e.g. Kammer et al., 2015), even if the macroscopic normal load is homogeneously applied. Such stress concentrations can cause a distorted local stress distribution like the ones shown in Figures 4d and 5e. Therefore, it can be considered that the basic features (e.g., location, duration, stability) of the long-term slow slip are derived from stress heterogeneity (generated by specimen geometry and loading configuration). Especially, the strong dependence of local slip evolution on the macroscopic shear loading (Table 2 and Figure A2) suggests a stable nature for the long-term slow slip. We suspect the reason is that the slow slip evolved toward the central area of the fault where the stored shear strain was relatively low (Figure 4d and Figure 5e), which could cause long-lasting slip evolution without immediate instability even on the fault with a velocity-weakening frictional property (in the framework of RSF). This is quite similar to the stable growth of non-interacting mode-I wing cracks under compression, where the flaw-induced mode-I stress intensity factor scales with the background loading but decreases with the length of the wing cracks (Ashby & Sammis, 1990). In addition, we also consider that the rheological property of fault rocks can contribute to the long-lasting stable slip. According to the compiled data and the proposed physical model in Aharonov and Scholz (2018), the steady-state rock friction behaves as velocity strengthening up to a critical thermal velocity V_t (~ 10-100 μm/s), independent of the sign of the RSF parameter b-a. Beyond V_t, thermal heating effect will become evident. In our case, the rate of long-term slow slip seldom reached 100 μm/s, implying that the velocity-strengthening fault rheology could also act to impede the acceleration of the long-term slow slip. Similarly, a recent experimental study has also invoked the involvement of viscous-type dissipation for understanding the initial stable growth of nucleation front (Gvirtzman & Fineberg, 2021). All in all, we conclude that stress heterogeneity and fault rheological property are responsible

for generating the stable fault slip.

5.2 Accelerated slip following the coalescence of multiple slip patches

In the current experiments, precursory slow slip with much higher slip rate (several hundreds of μm/s) developed, following the coalescence of two long-term slow slip fronts. Apparently, the coalescence of multiple slip patches has the potential to cause accelerated slip. Indeed, similar phenomenon has been documented by numerical simulations (Fukuyama & Madariaga, 2000; Kaneko & Ampuero, 2011), by experimental studies on a laboratory fault along the antiplane direction (Fukuyama et al., 2018), and by natural observations of slow slip events on the Cascadia subduction zone (Bletery & Nocquet, 2020). Other similar examples include the sudden increase of fault slip during the surface breakout of a forward-propagating rupture, which can be considered as due to the coalescence of the forward-propagating rupture front with its backward-propagating mirror (Dieterich, 1979; Xu et al., 2015), and to a lesser extent, the coalescence of tensile and/or shear cracks during rock fracture experiments (Bobet & Einstein, 1998; Renard et al., 2019). The aforementioned phenomena may be explained by the intense stress concentrations between approaching rupture/crack tips and the subsequent rapid relaxation of those stress concentrations (Fukuyama & Madariaga, 2000). From a kinematic point of view, they may also be explained by applying a slip-length scaling relation to an increased patch length (Dieterich, 1979; Bletery & Nocquet, 2020), or by invoking the full-crack and half-crack models (Xu et al., 2015). Given the above examples under a variety of conditions, it appears that the coalescence of multiple slip patches (or multiple cracks) through an increased range of elastic interaction could serve as a generic mechanism to cause large events and unstable failure.

5.3 Asperity and loading rate on it

The detected repeating foreshocks suggest that small asperities, which could slip unstably and radiate seismic waves, persistently existed and repeatedly slipped in a similar way on the fault surface over the current four experiments (Figures 2b, 2e, 2h, and 2k). We presume that those asperities originated from tiny topographic undulations on the fault at first. Stress concentration around the undulations facilitated the generation of wear materials (fault grooves and gouge) during frictional slip, which could further enhance the degree of stress concentration via a positive feedback loop (Yamashita et al., 2015). Consequently, some gouge bumps may have already been formed during the previous experiments on the fault surface, and they could play the role of seismic asperities especially for relatively large foreshocks. In fact, well-correlated distributions of generated gouge and hypocenters of small seismic events have been reported in a previous study (Yamashita et al., 2021), and hence can support our above presumption.

Unfortunately, AS output is not calibrated in the current study and therefore the absolute seismic scale cannot be obtained. As an alternative, below we roughly estimate the foreshock magnitude by referring to previous studies. Regarding the foreshock-like seismic events observed on a meter-scale laboratory fault, it

has been reported that their typical moment magnitude ranged from -7.0 to -5.0 (McLaskey et al., 2014; Yamashita et al., 2021). We consider that the foreshocks observed during the current experiments fall into a similar range of magnitude. By applying the Brune's model (Brune, 1970),

$\sigma = \frac{7}{16} M_0 r^{-3}$ (1),

with the definitions of seismic moment M_0 as

$M_0 = \mu D (\pi r^2)$ (2)

and moment magnitude (M_w) becomes

$M_w = \frac{2}{3} \log_{10} (M_0) - 6.067$ (3),

where Δ is the stress drop, r is the source radius, D is an average seismic slip, and is the shear modulus (39.3 GPa) calculated from the Young's modulus and the Poisson's ratio in Table 1. A typical D for a foreshock in the current experiments ranges from 0.048 m to 0.48 m. Here we assumed Δ of 1 MPa, which is the standard value for seismic events observed in a previous meter-scale experiment also using metagabbro specimens (Yamashita et al., 2021). Even for the largest possible foreshock in the current study ($M_w \sim$ -4.4, when r equals half fault width, 0.05 m with the assumption of Δ of 1 MPa), D equals only 0.93 µm. Considering these significantly small amounts of D relative to the accumulated slip shown in Figures7a and 7b, the asperities that hosted foreshocks could not be locked completely but probably slipped stably/episodically at their periphery during the long-term slow slip.

Before discussing the observed relationship between local slow slip rate and foreshock activity, the physical meaning of local slip rate should be clarified. Recalling the interpolated slip rate $\dot{D}_{\mathrm{loc}}$ at the site of asperity, it is natural to consider that $\dot{D}_{\mathrm{loc}}$ was not exactly the same as the actual slip rate on the asperity (which was partially locked at the time). In this sense, the local slip rate in the region surrounding the asperity should be a proxy of local loading rate applied to the asperity. For the above reason, we mainly use the term "local loading rate" to discuss the influence on foreshock activity in the following sections.

5.4 Dependence of foreshock occurrence on local loading rate

To understand the positive correlation between $\dot{D}_{\mathrm{loc}}$ (as a proxy of local loading rate) and the foreshock occurrence (Figures 7c, 7d, and 8), it is crucial to investigate the critical nucleation length h^* and its dependence on other parameters. In the framework of RSF law (Dieterich, 1992), h^* can be expressed as

$h^* = \frac{\mu D_c}{\sigma(b-a)}$ (4),

where D_{c} is the characteristic slip distance over which friction evolves and b-a is the frictional parameter that controls the slip stability with a change in slip velocity. It should be noted that h^* is inversely proportional to . According to Urata et al. (2017), the estimated values of RSF parameters b-a and D_{c} for a meter-scale metagabbro laboratory fault are 0.0014 and 0.3 µm, respectively.

Inserting these values into Eq. (4) results in an h^* value of 2.1 m under 4-MPa-normal stress, which seems consistent with the macroscopic slip behavior (Figures 4c, 7c, and 7d). If we assume that the real contact area on the fault is 1/1000 to 1/100 of the nominal fault area (Dieterich & Kilgore, 1996), which corresponds to a local normal stress on the asperity of 100 to 1000 times of the macroscopic one, and if we also assume that Eq. (4) is still applicable to the real contact area, then the local h^* becomes 2.1 to 21 mm, which is comparable to the asperity size (5.2 to 52 mm in diameter for M_{w} from -7.0 to -5.0, respectively, under the assumption of Δ of 1 MPa) in the current experiments. Although the theoretical expression of h^* is still under investigation in the presence of stress/frictional heterogeneity, a recent numerical simulation has shown that the above discussion is reasonable (Schaal & Lapusta, 2019).

Besides the dependence on normal stress, it has also been shown by both experimental (e.g. Guérin-Marthe et al., 2019; Kato et al., 1992; Xu et al., 2018) and numerical studies (e.g. Kaneko et al., 2016) that h^* can shrink with the increase of loading rate. We also consider that the local loading rate on an asperity increased with the slip rate in the surrounding region, which could shrink the h^* of the asperity and hence could promote an unstable slip (Figure 10). This scenario is similar to the one studied by McLaskey and Yamashita (2017). Furthermore, it is also supported by the results of a recent numerical simulation (Schaal & Lapusta, 2019), the transient behaviors of seismicity modulated by a nearby major earthquake (Cheng & Ben-Zion, 2019; Hatakeyama et al., 2017), and the correlation between local slip rate and tremor activity on the Cascadia subduction zone (Bartlow et al., 2011).

We also consider the rheological property (Aharonov & Scholz, 2018) mentioned in section 5.1 as a possible alternative mechanism for the foreshock occurrence at high local loading rate. The velocity-strengthening friction below the thermal velocity V_t can help store elastic energy on the asperities, which later can be rapidly released during the transition to velocity-weakening friction when local slip rate crosses V_t. The sudden increase in the number of foreshocks shown in Figure 8 might be related to the transition of frictional regime.

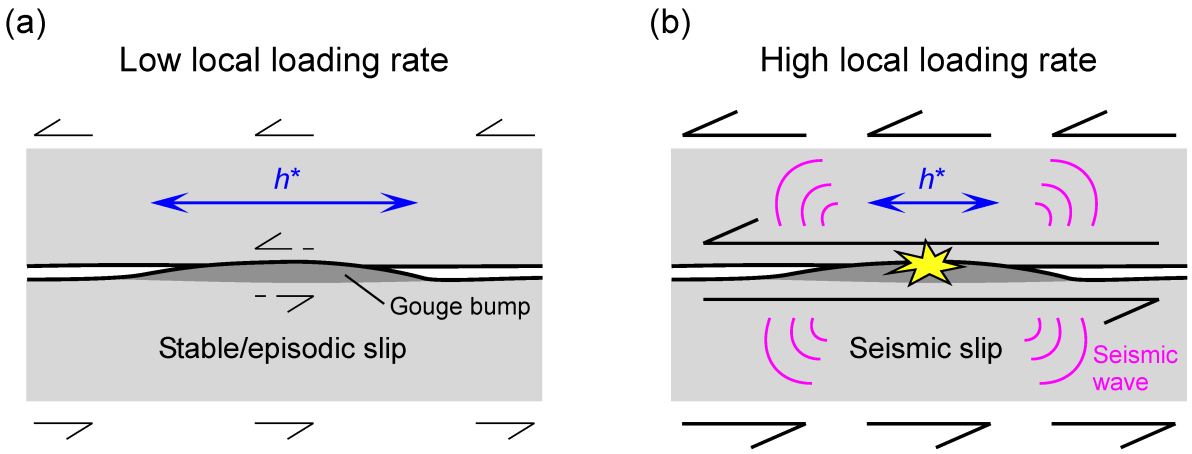

Figure 10. Schematic illustration of foreshock activity controlled by local loading rate. (a) Case for low local loading rate. The contacting asperity made of gouge bump could slip stably or episodically, because the critical nucleation length h^* is comparable to or larger than the asperity size. (b) Case for high local loading rate. The asperity can slip abruptly and seismically because h^* shrinks and becomes smaller than the asperity size due to the fast loading.

5.5 Dependence of foreshock magnitude on local loading rate

The current experimental results clearly show a positive correlation between the foreshock magnitude and the local loading rate (Figures 9b, 9d, and 9e), except for Group B (Figure 9c). We suspect that the lack of a clear correlation in Group B could be derived from a change in the size of relevant asperities between the experiments FB02-006 and FB02-010. We also note that Figure 9c actually shows a positive correlation within each experiment (in FB02-006 or in FB02-010), which suggests that the size of asperities might not change during each experiment and the dependence of foreshock magnitude on the local loading rate is still valid.

Considering the definition of seismic moment expressed in Eq. (2), either the amount of seismic slip or the source dimension needs to increase with the local loading rate, in order to match the positive correlation between the foreshock magnitude and the local loading rate. In fact, a previous experimental study has shown that high loading rate not only can enhance the efficiency for accumulating stress during the shear loading stage (by suppressing concurrent diffusional process such as aseismic slip), but also can promote more efficient energy release during the slip stage (Xu et al., 2018). Similarly, a numerical study of repeating earthquakes has shown that high loading rate can enlarge the source region for accumulating slip deficit, which ultimately will lead to a larger co-seismic rupture area as well as a larger amount of co-seismic slip (Yoshida et al., 2015). While we could not reveal the individual change(s) in foreshock

source properties (slip, source area) by our current instrumentations, we think the loading rate effects mentioned above may apply to our experiments. We will continue the investigation of the relation between foreshock magnitude and loading rate in our future studies. Especially, denser acoustic and displacement sensor arrays and direct imaging technique can help achieve a more complete understanding of the topic.

5.6 Implications for natural earthquake sequences

Elevated seismicity rate and its migration before and after a large earthquake are sometimes detected and reported in nature (e.g. Kato et al., 2012; Peng & Zhao, 2009). It is often interpreted that those seismic activities are driven by the propagation of aseismic slow slip and they occur at the slip front. However, if the situation in nature is similar to that in the current experiments, the slip front would have already passed through a potential asperity and then the associated seismic event on it may be activated by the surrounding slip with an elevated rate. In other words, the migration front of seismicity could lag behind the actual slow slip front (see also the discussion in Bartlow et al. (2011)), which would then support the idea of treating asperities as strong-but-brittle sticky spots — an equivalent term used in the field of icequakes (Podolskiy & Walter, 2016, and references therein). If that is the case, using the observed seismic events to estimate the actual slow slip front may cause some errors. Further investigation of the space-time relation between the seismic events and the slow slip will be needed in nature and laboratory.

As another example, creep or slow slip on a tectonic fault are often estimated based on the activities of repeating earthquakes (Uchida, 2019; Uchida & Bürgmann, 2019, and references therein). In those analyses, it is basically assumed that the asperities hosting repeating earthquakes are locked during the stick phase and the related seismic moment positively scales with the recurrence interval. However, if the seismic moment can be influenced by the local loading rate as shown by the current study, the estimated amount of creep or slow slip may contain some errors, especially for the situation right before or after a major earthquake, where locally elevated loading rate can decrease the recurrence interval and increase the magnitude of repeating earthquakes. Therefore, the analytical/empirical method(s) for analyzing repeating earthquakes may need to be improved by taking into account the effect of local loading rate.

6 Conclusions

We have conducted rock friction experiments using a newly developed large-scale apparatus that can shear 4-m-long rock specimens. We gradually increased shear load with normal stress kept at around 4 MPa, and observed many stick-slip events. The local displacement data showed that slips individually initiated from both the leading and trailing edges and kept propagating toward the central fault area during the long shear loading stage in each stick-slip cycle. After the coalescence of two long-term slow slip fronts, faster slow slip as part of the

nucleation process began at the central fault area and eventually led to main fast rupture over the fault. FEM calculation confirmed that the basic features of the long-term slow slip were derived from stress heterogeneity generated by the experimental configuration. Examination of foreshock activity and local slip data showed that foreshocks could occur regardless of the amount of accumulated slip. On the other hand, foreshocks were often observed when the local slip rate reached around 100 m/s during the nucleation process. We propose that there exist asperity areas on the fault, whose size is similar to the local critical nucleation length h^*. Those asperities slip stably when the local loading rate is low, but can also slip unstably and radiate seismic waves when the local loading rate becomes high, due to the shrinkage of h^* by the fast loading. We also found a clear positive correlation between the relative magnitude of repeating foreshocks and the local loading rate. Our results suggest that the local loading rate has a significant influence on the occurrence and magnitude of foreshocks. Therefore, its effect should be taken into account during the studies of earthquake nucleation process and other similar phenomena such as Episodic Tremor and Slip (ETS), icequakes, and repeating earthquakes.

Appendix A: Fault slip activity

A.1 Onset of main fast slip

To discuss the slip behaviors preceding the main fast fault rupture, the onset of the fast slip needs to be specified. We determined it based on the slip acceleration. We first low-pass filtered the slip data with a cut-off frequency of 5 kHz to remove the high-frequency noise, and then calculated the first- and second-time derivatives of the slip for obtaining the slip velocity and acceleration, respectively. We considered the time when the acceleration first exceeded a threshold as the beginning of the fast slip. In this study, we used six times the standard deviation, which was obtained from the slip acceleration in the stable period, as the threshold. We searched for the time in each channel and regarded the earliest time in all channels as the onset of the main fast slip. Figure A1 shows an example for the detected onset of the fast slip.

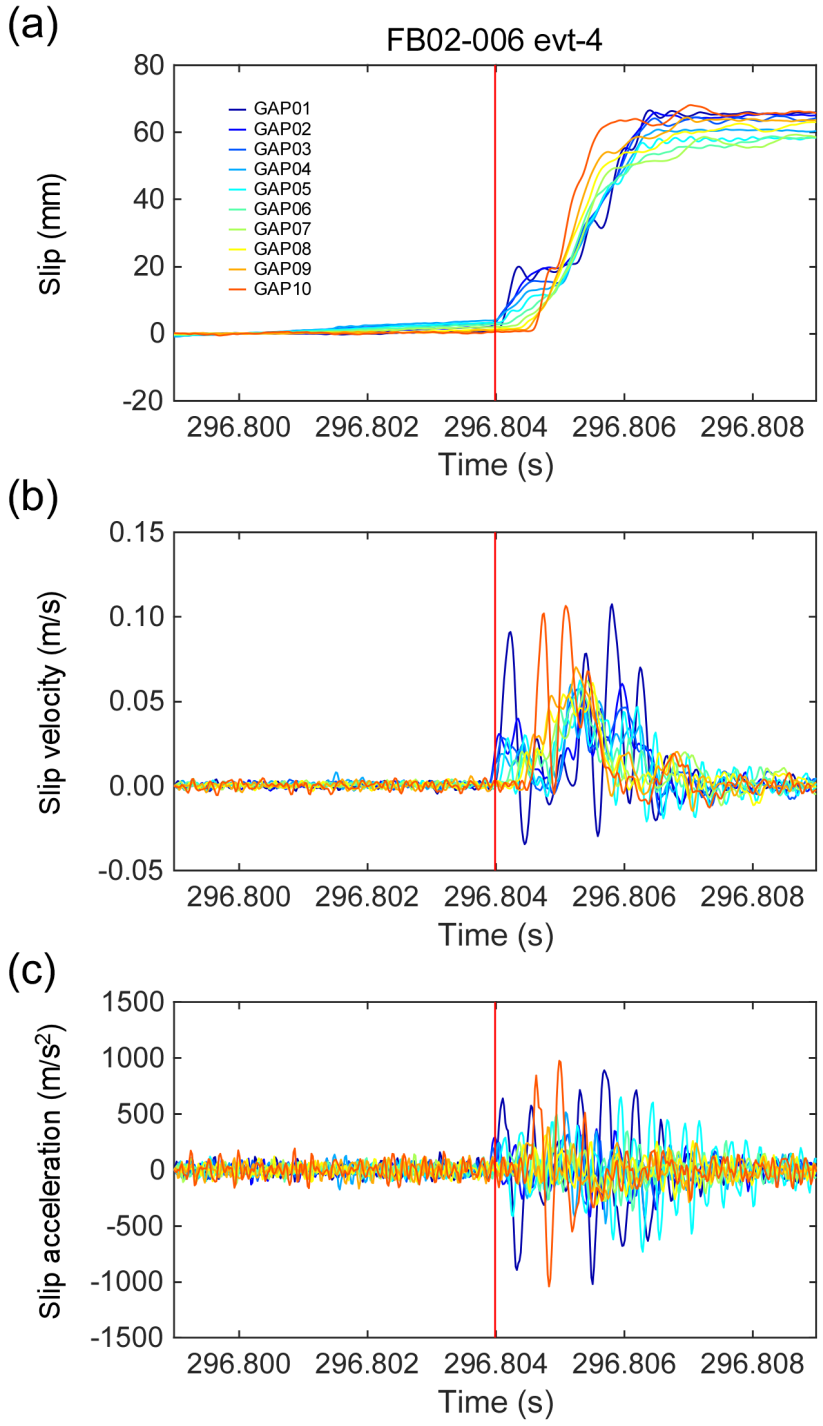
(a)
FB02-006 evt-4
Slip (mm)
80
60
40
20
0
-20
GAP01
GAP02
GAP03
GAP04
GAP05
GAP06
GAP07
GAP08
GAP09
GAP10
296.800
296.802
296.804
296.806
296.808
Time (s)
(b)
Slip velocity (m/s)
0.15
0.10
0.05
0.00
-0.05
296.800
296.802
296.804
296.806
296.808
Time (s)
(c)
Slip acceleration (m/s²)
1500
1000
500
0
-500
-1000
-1500
296.800
296.802
296.804
296.806
296.808
Time (s)

Figure

A1. Detection of the onset of the main fast slip. (a) Slip, (b) slip velocity, and (c) slip acceleration before and during a stick-slip event evt-4 in FB02-006. The slip data was low-pass filtered with a cut-off frequency of 5 kHz before calculating the velocity and the acceleration. The specified moment of the onset of the main fast slip is indicated with the vertical red line in (a), (b), and (c).

A.2 Dependence of long-term slow slip on shear loading

Since the shear load was manually built up, it was unsmooth and sometimes suspended during the loading, which is pronounced in the slow-loading experiments (Figures 2d and 2j). Figure A2a is a close-up view that shows such a temporal suspension of the shear loading in a time period much before the stick-slip event (Figure 2j). Figure A2b shows the slip data at both the edges (GAP01, GAP02, and GAP10) during the same time period as Figure A2a, and it also shows temporally-slowed slip evolution synchronized with the temporal suspension of shear loading. Clear positive correlations between the macroscopic shear loading rate and the local slip rate at GAP01 can be seen in Table 2 too. These features suggest a strong dependence of the long-term slow slip on the shear loading.

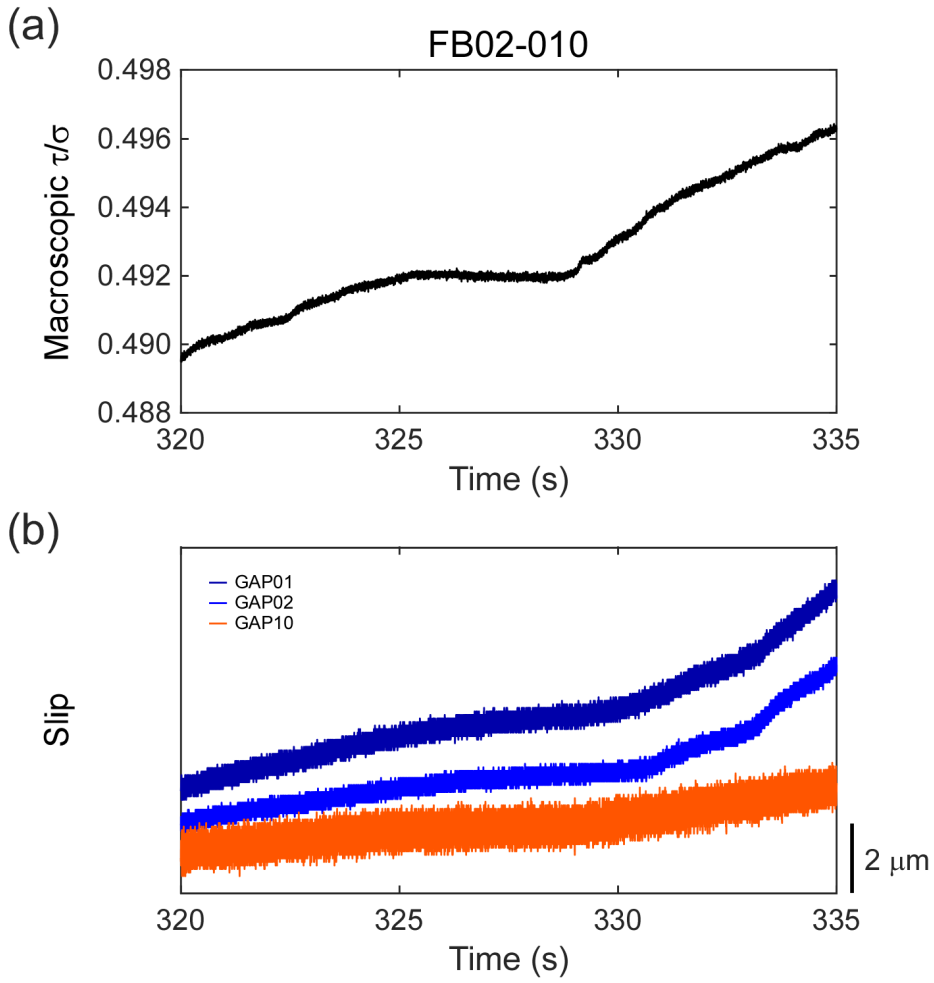

Figure A2. (a) Temporal suspension of shear loading during FB02-010. The intermittent shear loading is caused by the manual pumping. (b) Behavior of local slip at GAP01, GAP02, and GAP10 during FB02-010. The time period is the same as Figure A2a. The increasing rate of slip is slowed down during the temporal suspension of shear loading.

A.3 Local slip rate $\dot{D}_{\mathrm{loc}}$

In order to quantitatively investigate the relationship between the local slip rate and the foreshock occurrence, we estimate the amount of local slip rate at the same site and time as the foreshock. Figure A3 shows the records of GAP for 1 ms before and after the occurrence of a foreshock sevt-20 in FB02-006. In this case, the foreshock was located between GAP03 and GAP04. We fitted a linear line to each record for 2 ms at both neighboring GAP stations

and determined each trend, which corresponds to the slip rate at each GAP station. We then linearly interpolated the slip rate at the foreshock hypocenter under the assumption of one-dimensional slip distribution along the fault. Since slip data at both neighboring GAP stations are needed for this estimation, the local slip rate for the foreshock that occurred outside of GAP array was not estimated. We name this spatially-interpolated local slip rate $\dot{D}_{\mathrm{loc}}$. Figure 8 shows a histogram of foreshocks as a function of $\dot{D}_{\mathrm{loc}}$.

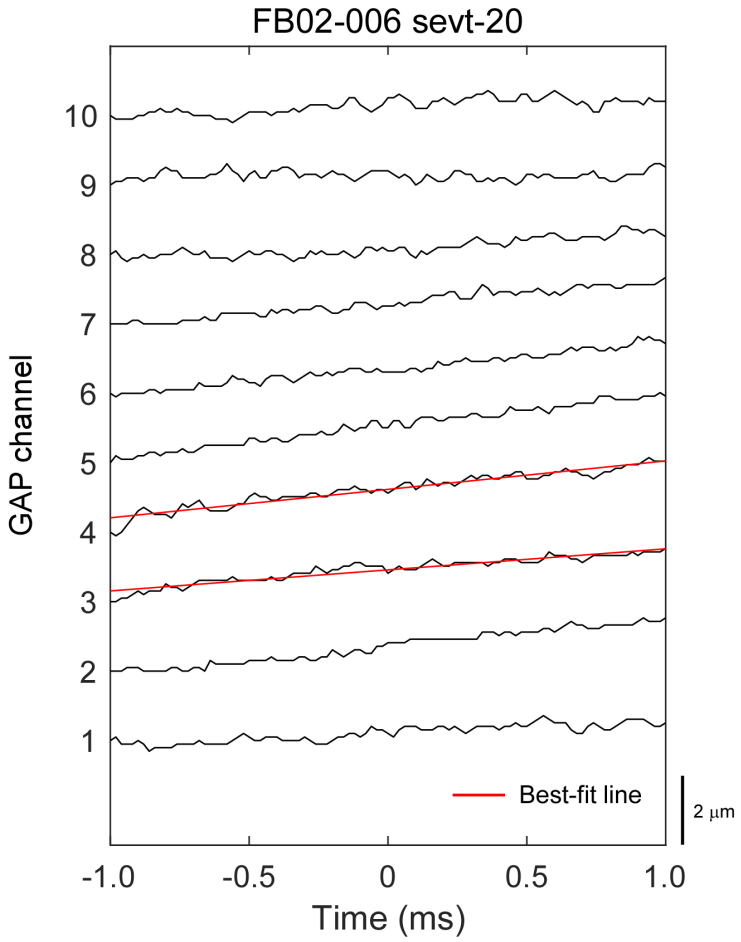

Figure A3. An example of estimation of local slip rate related to a seismic event. This panel shows the local slip data for 1 ms before and after the occurrence of a seismic event sevt-20 in FB02-006. The local slip rate at the same site and time as the seismic event is estimated from linear interpolation of the best-fit trends for the slip data at the neighboring slip sensors as shown by red lines.

Appendix B: Seismic activity

B.1 Hypocenter and size of seismic events

Based on the seismic record, we determined the origin time and hypocenter location of the foreshocks. We first specified the time when a foreshock occurred by referring to local peaks of the sum of squared AS amplitude (Figure B1b). We next picked up the time-window for each foreshock as shown in Figure 3, and then picked the arrival times of seismic waves. For the picking, we did not use AS waveform but used SGT waveform, because AS array is sparse relative to SGT array and the arrival of S wave was clearer for the record of SGT as shown in Figure 3. After picking the arrival time of S wave at each station, we conducted a grid search to determine the origin time and the location of hypocenter. We searched for the optimum parameters including the wave velocity (V), so that the following L^2 norm becomes minimum:

$L^2 = \sum_{i=1}^{N} \left(t_i - t_0 - \frac{D_i}{V} \right)^2$ (B.1),

where N is the number of SGT stations, t_{i} is the arrival time at i-th SGT station, t_0 is the origin time, and D_{i} is the distance between the hypocenter (x_0, y_0, z_0) and the location of i-th SGT station (x_{i}, y_{i}, z_{i}) as follow:

$D_i = \sqrt{(x_i - x_0)^2 + (y_i - y_0)^2 + (z_i - z_0)^2}$ (B.2).

In this search, we assumed that the foreshocks occurred on the fault surface (i.e. z_0=0). After locating the hypocenter, we estimated the magnitude of the foreshock based on the amplitudes of AS. Unfortunately, we could not calibrate the response of AS sensor. Instead, we estimated a laboratory-specific magnitude M_{Lab} following Zang et al. (1998):

$M_{\mathrm{Lab}} = \log_{10} A$ (B.3), and

$A = \sqrt{\frac{1}{K} \sum_{i=1}^{K} \left(\frac{r_i}{10} A_{i_{\max}} \right)^2}$ (B.4),

where K is the number of AS stations, r_i is the distance between the hypocenter and i-th AS station in mm, and $A_{i_{\max}}$ is the maximum amplitude of seismic wave at i-th AS station in volt. $A_{i_{\max}}$ is mainly derived from S wave. The estimated hypocenters and M_{Lab} values of foreshocks are shown in Figure 6.

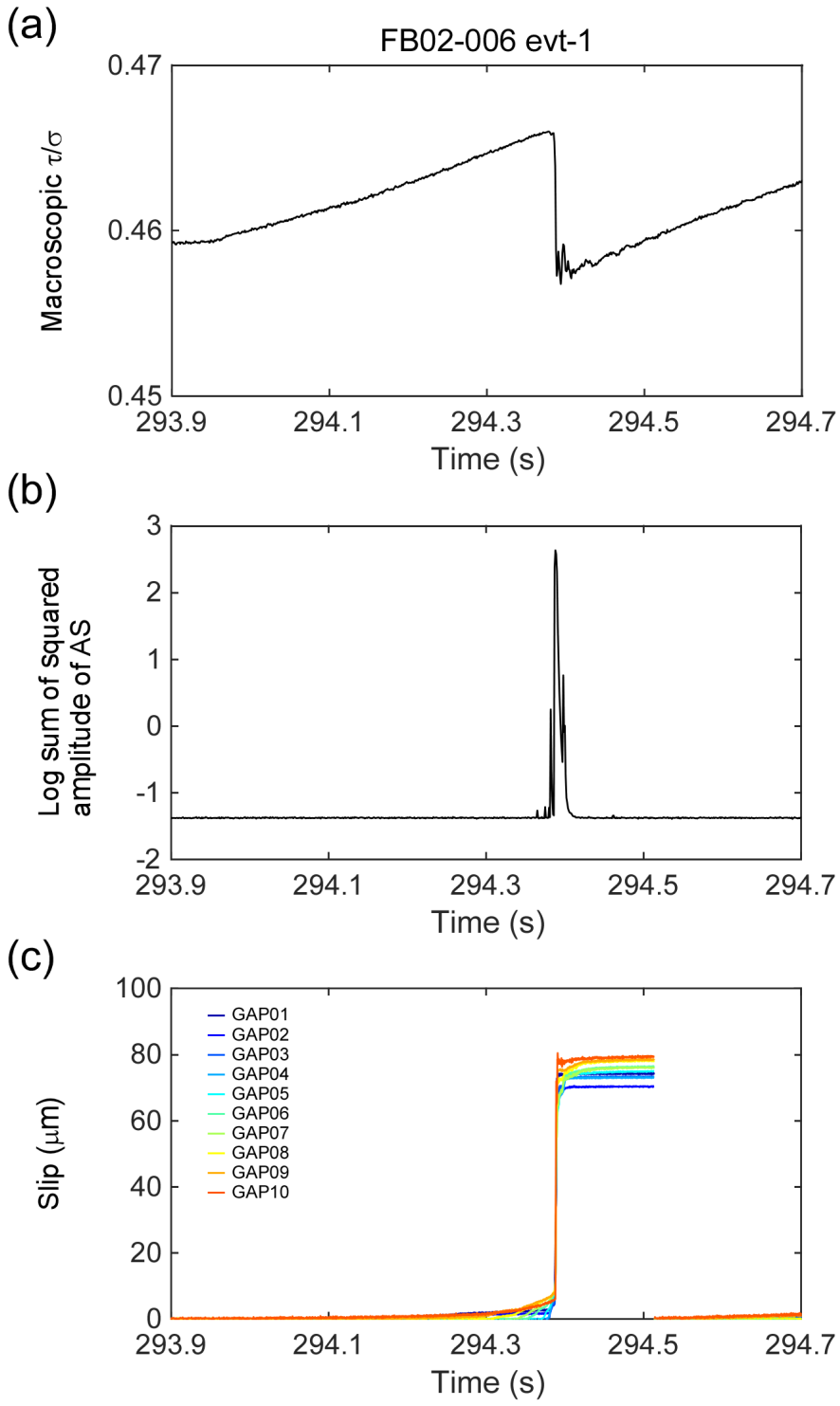
(a)
FB02-006 evt-1
Macroscopic τ/σ
0.47
0.46
0.45
293.9
294.1
294.3
294.5
294.7
Time (s)
(b)
Log sum of squared amplitude of AS
3
2
1
0
-1
-2
293.9
294.1
294.3
294.5
294.7
Time (s)
(c)
Slip (μm)
100
80
60
40
20
0
GAP01
GAP02
GAP03
GAP04
GAP05
GAP06
GAP07
GAP08
GAP09
GAP10
293.9
294.1
294.3
294.5
294.7
Time (s)

Figure

B1. Close-up view of (a) Macroscopic / , (b) logarithmic sum of squared amplitude of AS output, and (c) the amount of slip for experiment FB02-006 evt-1.

B.2 Matched filter technique

Matched filter technique (MFT) is an effective means for detecting a seismic event whose hypocenter and focal mechanism are close to those of a template event. MFT scans a continuous seismic record and detects similar waveforms to the template waveforms. This technique has been widely used for detecting various seismic events such as low-frequency earthquakes (Shelly et al., 2007), aftershocks (Peng & Zhao, 2009), and foreshocks (Kato et al., 2012).

For applying MFT, we first need to determine template foreshocks. We searched for groups producing more than five foreshocks within 15 mm of relative hypocentral distances, and then defined the foreshock with the largest M_{Lab} (whose signal-to-noise ratio should be high) in each group as the template foreshock. We excluded one template foreshock whose signals saturated in many AS stations. As a result, we found four template foreshocks in total and named them template A, B, C, and D. The hypocenters of the template foreshocks are shown in Figure 6. As the template waveforms for scanning, we used a 0.25-ms-long time window beginning 0.05 ms prior to the estimated S wave arrival time. The waveforms of template foreshock D are displayed in Figure B2 as an example. By using the four sets of the template waveforms, we scanned throughout the continuous seismic records of four experiments. We computed correlation coefficients between the template waveforms and those in the seismic records with shifting one data point (10^{-7} s). The calculated correlation coefficients were averaged over all station channels at each step. We set two thresholds to detect a repeating foreshock: (1) the averaged correlation coefficient normalized by standard deviation is more than 8, and (2) the averaged correlation coefficient is more than 0.3. As a result, we detected 3, 5, 6, and 9 repeating foreshocks for template A, B, C, and D, and then named them Group A, B, C, and D, respectively. An example for the waveforms of a detected repeating foreshock is shown in Figure B2. The cross symbols in Figures 2b, 2e, 2h, and 2k represent the occurrence times of the repeating foreshocks in each group. The results suggest that the repeating foreshocks did not recur during a single stick-slip cycle but were activated before different main stick-slip events. The detailed information of the repeating foreshocks is shown in Table B1.

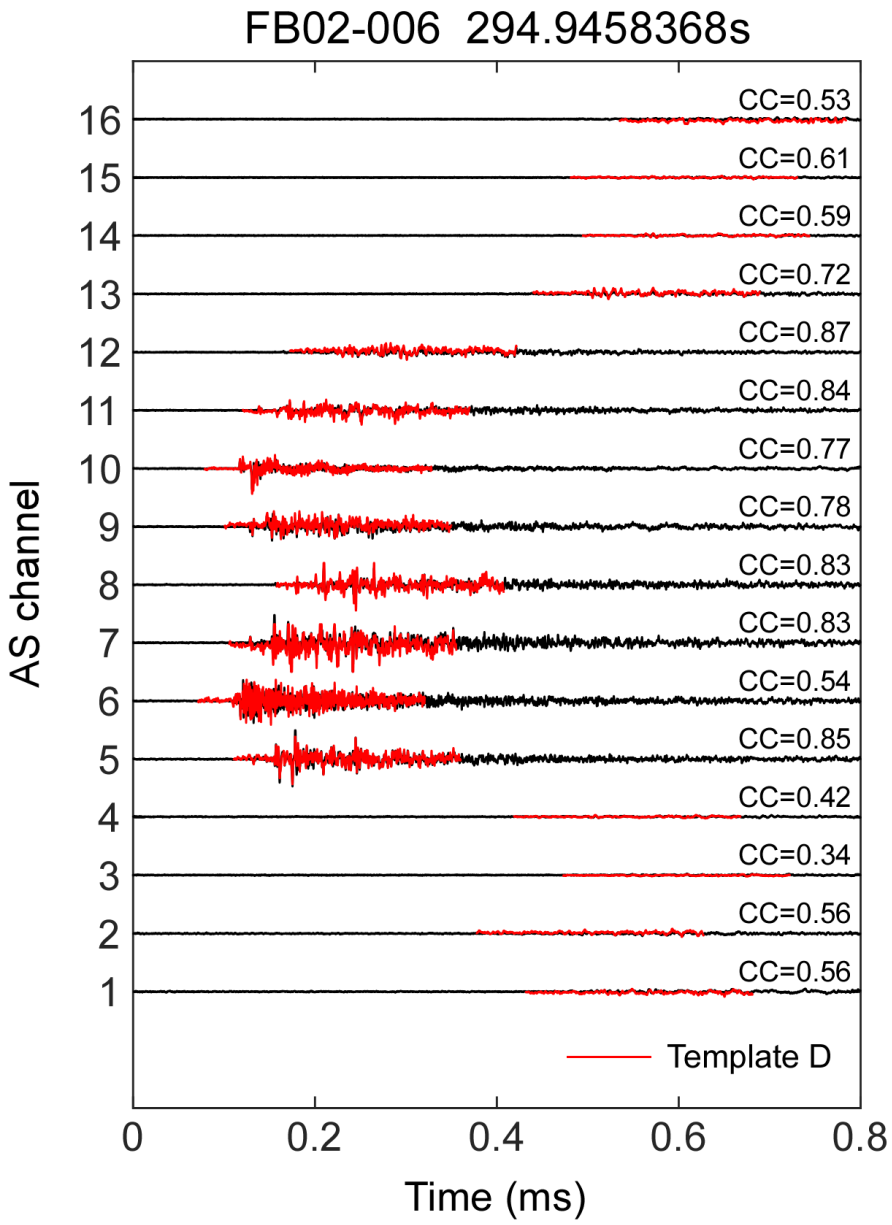

Figure B2. An example of a detected repeating foreshock event by the matched filter technique. Waveforms for the template foreshock D are overlaid with red lines on those for the detected repeating foreshock. Amplitudes are normalized by the maximum amplitude in all channels.

Group	X (m)*	Y (m)**	ID	Experiment ID	Time (s)	M_r	Proportion***	$\dot{D}_{loc}$ (μm/s)
A	2.639	0.065	1	FB02-006	296.3303582	-0.932	0.98	310.3
			2	FB02-007	821.1738689	0.179	0.89	2374.9
			3	FB02-007	841.3512460	0	1	2097.2
B	1.371	0.064	1	FB02-006	294.9423958	-0.770	0.97	583.3
			2	FB02-006	298.9895940	-0.738	0.97	787.5
			3	FB02-006	300.5599234	-0.642	0.90	661.4
			4	FB02-010	230.6809219	0	1	716.2
			5	FB02-010	264.6059238	-0.080	0.93	344.4
C	1.318	0.028	1	FB02-006	296.8006003	-0.160	0.84	1017.4
			2	FB02-006	298.3732842	-0.302	0.81	1601.5
			3	FB02-006	298.9958516	-0.851	0.94	330.8
			4	FB02-007	799.4798362	-0.390	0.87	685.6
			5	FB02-010	230.6815791	0	1	1280.0
			6	FB02-010	264.6074621	0.326	0.84	1045.9
D	1.885	0.033	1	FB02-006	294.9459368	-0.267	0.91	577.5
			2	FB02-007	727.8334448	-0.087	0.89	482.6
			3	FB02-007	799.4808790	-0.065	0.90	792.6
			4	FB02-007	841.3518215	0.116	0.81	620.5
			5	FB02-008	256.7321134	-0.239	0.90	554.3
			6	FB02-010	230.6831404	0.046	0.86	1460.0
			7	FB02-010	264.6069558	-0.123	0.89	371.2
			8	FB02-010	281.9832687	0	1	535.0
			9	FB02-010	347.0520783	0.131	0.96	897.5

Table B1 *Properties of repeating foreshocks*

*Distance from western edge of the upper specimen.

**Distance from southern edge of the upper specimen.

***Proportion of the variance for positive correlation of waveforms between template foreshock and repeating one to the total variance.

B.3 Relative magnitude of repeating foreshocks

For simple but robust estimation of the relative magnitude of repeating foreshocks, we directly compared the amplitudes of the observed waveforms in the time domain. For this comparison, we used the same data window as MFT, that is, the 0.25-ms-long time window beginning 0.05 ms prior to the S wave arrival time. According to a previous study (McLaskey et al., 2014) that used the same acoustic sensor (V103) as the current study, the sensor output is almost proportional to ground displacement in the frequency band of 30 kHz-1 MHz. Therefore, we band-pass filtered the waveforms of the template and the repeating foreshocks with that frequency band before the comparison. Figure B3 shows the AS output for the repeating foreshocks against that for the template foreshock at each AS station. Since all groups of the repeating foreshocks

were distributed around the central fault area (Figure 6), we only used the waveforms recorded by the central eight AS stations (AS05 to AS12). All data points recorded at the eight stations are stacked in each panel and used for the following analysis. The best-fit trend is equal to the amplitude ratio of the repeating foreshocks to the template one. This trend R should be roughly proportional to the ratio of the seismic moment of the repeating foreshock to that of the template foreshock. It should be noted that effects of geometric attenuation and instrumental responses are canceled out by taking the ratio. Considering the relation $M_w^{'} - M_w^{''} = \frac{2}{3}\log_{10}\left(\frac{M_0^{'}}{M_0^{''}}\right)$, where $M_w^{'}$ and $M_w^{''}$ are arbitrary moment magnitudes and $M_0^{'}$ and $M_0^{''}$ are associated seismic moments, respectively, from the definition of Eq. (3), common logarithm of R should scale with a relative magnitude of the repeating foreshock to the magnitude of template foreshock. We name it M_{r} and show the estimated values in Table B1. For the estimation of the trend, we applied a principal component analysis with two variables. Proportion of the variance for the first principal component (positive correlation of waveforms between the template foreshock and the repeating one) to the total variance, which indicates how well the distribution is explained by the associated relation, is high enough as shown in Table B1.

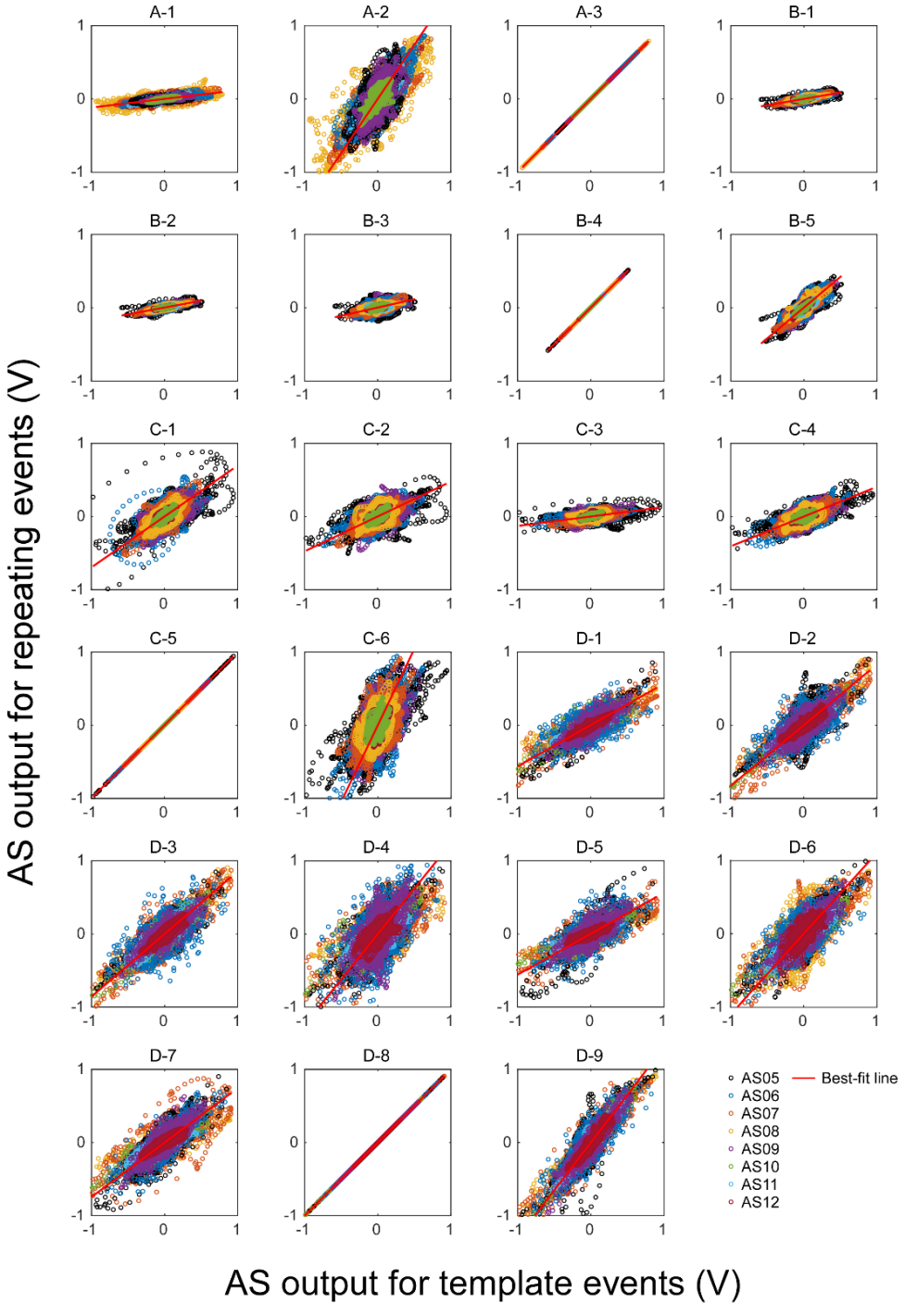
A-1
A-2
A-3
B-1
B-2
B-3
B-4
B-5
C-1
C-2
C-3
C-4
C-5
C-6
D-1
D-2
D-3
D-4
D-5
D-6
D-7
D-8
D-9
AS output for repeating events (V)
AS output for template events (V)
AS05
AS06
AS07
AS08
AS09
AS10
AS11
AS12
Best-fit line

Figure

B3. Band-pass filtered outputs of acoustic sensors (AS) for matched foreshocks against those for the template foreshocks. The records obtained at AS05 to AS12 are displayed and used for the estimation of relative waveform amplitude. Red linear line shows the best-fit trend estimated with the principal component analysis. The associated event ID is displayed above each panel. Note that A-3, B-4, C-5, and D-8 are the template foreshocks for each group.

Acknowledgments, Samples, and Data

The data presented in this study are available at http://doi.org/10.5281/zenodo.5513461. This study was supported by the NIED research project "Large Earthquake Generation Process" and JSPS Kakenhi Grant Numbers JP17H02954, JP16H06477, JP21H05201. S.X. acknowledges fund support by NSFC grant 42074048.

References

Aharonov, E., & Scholz, C. H. (2018). A Physics-Based Rock Friction Constitutive Law: Steady State Friction. *Journal of Geophysical Research: Solid Earth*, *123*(2), 1591–1614. https://doi.org/10.1002/2016JB013829Ampuero, J.-P., & Rubin, A. M. (2008). Earthquake nucleation on rate and state faults - Aging and slip laws. *Journal of Geophysical Research*, *113*(B1), B01302. https://doi.org/10.1029/2007JB005082Ashby, M. F., & Sammis, C. G. (1990). The damage mechanics of brittle solids in compression. *Pure and Applied Geophysics*, *133*(3), 489–521. https://doi.org/10.1007/BF00878002Bartlow, N. M., Miyazaki, S., Bradley, A. M., & Segall, P. (2011). Space-time correlation of slip and tremor during the 2009 Cascadia slow slip event. *Geophysical Research Letters*, *38*(18), n/a-n/a. https://doi.org/10.1029/2011GL048714Bletery, Q., & Nocquet, J.-M. (2020). Slip bursts during coalescence of slow slip events in Cascadia. *Nature Communications*, *11*(1), 2159. https://doi.org/10.1038/s41467-020-15494-4Bobet, A., & Einstein, H. H. (1998). Fracture coalescence in rock-type materials under uniaxial and biaxial compression. *International Journal of Rock Mechanics and Mining Sciences*, *35*(7), 863–888. https://doi.org/10.1016/S0148-9062(98)00005-9Bouchon, M., Durand, V., Marsan, D., Karabulut, H., & Schmittbuhl, J. (2013). The long precursory phase of most large interplate earthquakes. *Nature Geoscience*, *6*(4), 299–302. https://doi.org/10.1038/ngeo1770Brune, J. N. (1970). Tectonic stress and the spectra of seismic shear waves from earthquakes. *Journal of Geophysical Research*, *75*(26), 4997–5009. https://doi.org/10.1029/JB075i026p04997Cheng, Y., & Ben-Zion, Y. (2019). Transient Brittle-Ductile Transition Depth Induced by Moderate-Large Earthquakes in Southern and Baja California. *Geophysical Research Letters*, *46*(20), 11109–11117. https://doi.org/10.1029/2019GL084315Dieterich, J. H. (1978). Preseismic fault slip and earthquake prediction. *Journal of Geophysical Research*, *83*(B8), 3940–3948. https://doi.org/10.1029/JB083iB08p03940Dieterich, J. H. (1979). Modeling of rock friction: 2. Simulation of preseismic slip. *Journal of Geophysical Research*, *84*(B5), 2169–2175. https://doi.org/10.1029/JB084iB05p02169Dieterich, J. H., & Kilgore, B. D. (1996). Imaging surface contacts: power law contact distributions and contact stresses in quartz, calcite, glass and acrylic

plastic. *Tectonophysics*, *256*(1–4), 219–239. https://doi.org/10.1016/0040-1951(95)00165-4Dieterich, J. H. (1992). Earthquake nucleation on faults with rate-and state-dependent strength. *Tectonophysics*, *211*(1–4), 115–134. https://doi.org/10.1016/0040-1951(92)90055-BFukuyama, E., & Madariaga, R. (2000). Dynamic Propagation and Interaction of a Rupture Front on a Planar Fault. In P. Mora, M. Matsu'ura, R. Madariaga, & J.-B. Minster (Eds.), *Microscopic and Macroscopic Simulation: Towards Predictive Modelling of the Earthquake Process* (pp. 1959–1979). Basel: Birkhäuser Basel. https://doi.org/10.1007/978-3-0348-7695-7_9Fukuyama, E., Mizoguchi, K., Yamashita, F., Togo, T., Kawakata, H., Yoshimitsu, N., et al. (2014). Large-scale Biaxial Friction Experiments Using a NIED Large-scale Shaking Table. *Report of the National Research Institute for Earth Science and Disaster Prevention*, *81*(81), 15–35.Fukuyama, E., Tsuchida, K., Kawakata, H., Yamashita, F., Mizoguchi, K., & Xu, S. (2018). Spatiotemporal complexity of 2-D rupture nucleation process observed by direct monitoring during large-scale biaxial rock friction experiments. *Tectonophysics*, *733*, 182–192. https://doi.org/10.1016/j.tecto.2017.12.023Guérin-Marthe, S., Nielsen, S., Bird, R., Giani, S., & Di Toro, G. (2019). Earthquake Nucleation Size: Evidence of Loading Rate Dependence in Laboratory Faults. *Journal of Geophysical Research: Solid Earth*, *124*(1), 689–708. https://doi.org/10.1029/2018JB016803Gvirtzman, S., & Fineberg, J. (2021). Nucleation fronts ignite the interface rupture that initiates frictional motion. *Nat. Phys.* *17*, 1037–1042. https://doi.org/10.1038/s41567-021-01299-9Hatakeyama, N., Uchida, N., Matsuzawa, T., & Nakamura, W. (2017). Emergence and disappearance of interplate repeating earthquakes following the 2011 M 9.0 Tohoku-oki earthquake: Slip behavior transition between seismic and aseismic depending on the loading rate. *Journal of Geophysical Research: Solid Earth*, *122*(7), 5160–5180. https://doi.org/10.1002/2016JB013914Ito, Y., Hino, R., Kido, M., Fujimoto, H., Osada, Y., Inazu, D., et al. (2013). Episodic slow slip events in the Japan subduction zone before the 2011 Tohoku-Oki earthquake. *Tectonophysics*, *600*, 14–26. https://doi.org/10.1016/j.tecto.2012.08.022Kammer, D. S., Radiguet, M., Ampuero, J.-P., & Molinari, J.-F. (2015). Linear Elastic Fracture Mechanics Predicts the Propagation Distance of Frictional Slip. *Tribology Letters*, *57*(3), 23. https://doi.org/10.1007/s11249-014-0451-8Kaneko, Y., & Ampuero, J.-P. (2011). A mechanism for preseismic steady rupture fronts observed in laboratory experiments. *Geophysical Research Letters*, *38*(21), n/a-n/a. https://doi.org/10.1029/2011GL049953Kaneko, Yoshihiro, Nielsen, S. B., & Carpenter, B. M. (2016). The onset of laboratory earthquakes explained by nucleating rupture on a rate-and-state fault. *Journal of Geophysical Research: Solid Earth*, *121*(8), 6071–6091. https://doi.org/10.1002/2016JB013143Kato, A., Obara, K., Igarashi, T., Tsuruoka, H., Nakagawa, S., & Hirata, N. (2012). Propagation of Slow Slip Leading Up to the 2011 Mw 9.0 Tohoku-Oki Earthquake. *Science*, *335*(6069), 705–708. https://doi.org/10.1126/science.1215141Kato, N., Yamamoto, K., Yamamoto, H., & Hirasawa, T. (1992). Strain-rate effect

on frictional strength and the slip nucleation process. *Tectonophysics*, *211*(1–4), 269–282. https://doi.org/10.1016/0040-1951(92)90064-DKe, C.-Y., McLaskey, G. C., & Kammer, D. S. (2018). Rupture Termination in Laboratory-Generated Earthquakes. *Geophysical Research Letters*, *45*(23), 12,784-12,792. https://doi.org/10.1029/2018GL080492Lapusta, N., & Rice, J. R. (2003). Nucleation and early seismic propagation of small and large events in a crustal earthquake model. *Journal of Geophysical Research: Solid Earth*, *108*(B4). https://doi.org/10.1029/2001JB000793Latour, S., Schubnel, A., Nielsen, S., Madariaga, R., & Vinciguerra, S. (2013). Characterization of nucleation during laboratory earthquakes. *Geophysical Research Letters*, *40*(19), 5064–5069. https://doi.org/10.1002/grl.50974McLaskey, G. C. (2019). Earthquake Initiation From Laboratory Observations and Implications for Foreshocks. *Journal of Geophysical Research: Solid Earth*, *124*(12), 12882–12904. https://doi.org/10.1029/2019JB018363McLaskey, G. C., & Kilgore, B. D. (2013). Foreshocks during the nucleation of stick-slip instability. *Journal of Geophysical Research: Solid Earth*, *118*(6), 2982–2997. https://doi.org/10.1002/jgrb.50232McLaskey, G. C., & Lockner, D. A. (2014). Preslip and cascade processes initiating laboratory stick slip. *Journal of Geophysical Research: Solid Earth*, *119*(8), 6323–6336. https://doi.org/10.1002/2014JB011220McLaskey, G. C., & Yamashita, F. (2017). Slow and fast ruptures on a laboratory fault controlled by loading characteristics. *Journal of Geophysical Research: Solid Earth*, *122*(5), 3719–3738. https://doi.org/10.1002/2016JB013681McLaskey, G. C., Kilgore, B. D., Lockner, D. A., & Beeler, N. M. (2014). Laboratory Generated M -6 Earthquakes. *Pure and Applied Geophysics*, *171*(10), 2601–2615. https://doi.org/10.1007/s00024-013-0772-9Nielsen, S., Taddeucci, J., & Vinciguerra, S. (2010). Experimental observation of stick-slip instability fronts. *Geophysical Journal International*, *180*(2), 697–702. https://doi.org/10.1111/j.1365-246X.2009.04444.xNoda, H., Nakatani, M., & Hori, T. (2013). Large nucleation before large earthquakes is sometimes skipped due to cascade-up-Implications from a rate and state simulation of faults with hierarchical asperities. *Journal of Geophysical Research: Solid Earth*, *118*(6), 2924–2952. https://doi.org/10.1002/jgrb.50211Ohnaka, M., & Kuwahara, Y. (1990). Characteristic features of local breakdown near a crack-tip in the transition zone from nucleation to unstable rupture during stick-slip shear failure. *Tectonophysics*, *175*(1–3), 197–220. https://doi.org/10.1016/0040-1951(90)90138-XOhnaka, M., & Shen, L. (1999). Scaling of the shear rupture process from nucleation to dynamic propagation: Implications of geometric irregularity of the rupturing surfaces. *Journal of Geophysical Research: Solid Earth*, *104*(B1), 817–844. https://doi.org/10.1029/1998JB900007Okubo, P. G., & Dieterich, J. H. (1984). Effects of physical fault properties on frictional instabilities produced on simulated faults. *Journal of Geophysical Research: Solid Earth*, *89*(B7), 5817–5827. https://doi.org/10.1029/JB089iB07p05817Peng, Z., & Zhao, P. (2009). Migration of early aftershocks following the 2004 Parkfield earthquake. *Nature Geoscience*, *2*(12), 877–881. https://doi.org/10.1038/ngeo697Podolskiy,

E. A., & Walter, F. (2016). Cryoseismology. *Reviews of Geophysics*, 54, 708–758, https://doi.org/10.1002/2016RG000526Renard, F., McBeck, J., Kandula, N., Cordonnier, B., Meakin, P., & Ben-Zion, Y. (2019). Volumetric and shear processes in crystalline rock approaching faulting. *Proceedings of the National Academy of Sciences*, *116*(33), 16234 LP – 16239. https://doi.org/10.1073/pnas.1902994116Rubin, A. M., & Ampuero, J.-P. (2005). Earthquake nucleation on (aging) rate and state faults. *Journal of Geophysical Research: Solid Earth*, *110*(B11), B11312. https://doi.org/10.1029/2005JB003686Ruiz, S., Metois, M., Fuenzalida, A., Ruiz, J., Leyton, F., Grandin, R., et al. (2014). Intense foreshocks and a slow slip event preceded the 2014 Iquique Mw 8.1 earthquake. *Science*, *345*(6201), 1165–1169. https://doi.org/10.1126/science.1256074Ruiz, S., Aden-Antoniow, F., Baez, J. C., Otarola, C., Potin, B., del Campo, F., et al. (2017). Nucleation Phase and Dynamic Inversion of the Mw 6.9 Valparaíso 2017 Earthquake in Central Chile. *Geophysical Research Letters*, *44*(20), 10,210-290,297. https://doi.org/10.1002/2017GL075675Schaal, N., & Lapusta, N. (2019). Microseismicity on Patches of Higher Compression During Larger-Scale Earthquake Nucleation in a Rate-and-State Fault Model. *Journal of Geophysical Research: Solid Earth*, *124*(2), 1962–1990. https://doi.org/https://doi.org/10.1029/2018JB016395Selvadurai, P. A., & Glaser, S. D. (2015). Laboratory-developed contact models controlling instability on frictional faults. *Journal of Geophysical Research: Solid Earth*, *120*(6), 4208–4236. https://doi.org/10.1002/2014JB011690Shelly, D. R., Beroza, G. C., & Ide, S. (2007). Non-volcanic tremor and low-frequency earthquake swarms. *Nature*, *446*(7133), 305–307. https://doi.org/10.1038/nature05666Socquet, A., Valdes, J. P., Jara, J., Cotton, F., Walpersdorf, A., Cotte, N., et al. (2017). An 8 month slow slip event triggers progressive nucleation of the 2014 Chile megathrust. *Geophysical Research Letters*, *44*(9), 4046–4053. https://doi.org/10.1002/2017GL073023Tape, C., Holtkamp, S., Silwal, V., Hawthorne, J., Kaneko, Y., Ampuero, J. P., et al. (2018). Earthquake nucleation and fault slip complexity in the lower crust of central Alaska. *Nature Geoscience*. https://doi.org/10.1038/s41561-018-0144-2Uchida, N. (2019). Detection of repeating earthquakes and their application in characterizing slow fault slip. *Progress in Earth and Planetary Science*, *6*(1), 40. https://doi.org/10.1186/s40645-019-0284-zUchida, N., & Bürgmann, R. (2019). Repeating Earthquakes. *Annual Review of Earth and Planetary Sciences*, *47*(1), 305–332. https://doi.org/10.1146/annurev-earth-053018-060119Uenishi, K., & Rice, J. R. (2003). Universal nucleation length for slip-weakening rupture instability under nonuniform fault loading. *Journal of Geophysical Research: Solid Earth*, *108*(B1), 2042. https://doi.org/10.1029/2001JB001681Urata, Y., Yamashita, F., Fukuyama, E., Noda, H., & Mizoguchi, K. (2017). Apparent Dependence of Rate- and State-Dependent Friction Parameters on Loading Velocity and Cumulative Displacement Inferred from Large-Scale Biaxial Friction Experiments. *Pure and Applied Geophysics*, *174*(6), 2217–2237. https://doi.org/10.1007/s00024-016-1422-9Xu, S., Fukuyama, E., Ben-Zion, Y., & Ampuero, J.-P. (2015).

Dynamic rupture activation of backthrust fault branching. *Tectonophysics*, *644–645*, 161–183. https://doi.org/10.1016/j.tecto.2015.01.011Xu, S., Fukuyama, E., Yamashita, F., Mizoguchi, K., Takizawa, S., & Kawakata, H. (2018). Strain rate effect on fault slip and rupture evolution: Insight from meter-scale rock friction experiments. *Tectonophysics*, *733*, 209–231. https://doi.org/10.1016/j.tecto.2017.11.039Yamashita, F., Fukuyama, E., Mizoguchi, K., Takizawa, S., Xu, S., & Kawakata, H. (2015). Scale dependence of rock friction at high work rate. *Nature*, *528*(7581), 254–257. https://doi.org/10.1038/nature16138Yamashita, F., Fukuyama, E., Xu, S., Mizoguchi, K., Kawakata, H., & Takizawa, S. (2018). Rupture preparation process controlled by surface roughness on meter-scale laboratory fault. *Tectonophysics*, *733*, 193–208. https://doi.org/10.1016/j.tecto.2018.01.034Yamashita, F., Fukuyama, E., Xu, S., Kawakata, H., Mizoguchi, K., & Takizawa, S. (2021). Two end-member earthquake preparations illuminated by foreshock activity on a meter-scale laboratory fault. *Nature Communications*, *12*(1), 4302. https://doi.org/10.1038/s41467-021-24625-4Yoshida, S., Kato, N., & Fukuda, J. (2015). Numerical simulation of the Kamaishi repeating earthquake sequence: Change in magnitude due to the 2011 Tohoku-oki earthquake. *Tectonophysics*, *651–652*, 44–57. https://doi.org/10.1016/j.tecto.2015.03.012Zang, A., Christian Wagner, F., Stanchits, S., Dresen, G., Andresen, R., & Haidekker, M. A. (1998). Source analysis of acoustic emissions in Aue granite cores under symmetric and asymmetric compressive loads. *Geophysical Journal International*, *135*(3), 1113–1130. https://doi.org/10.1046/j.1365-246X.1998.00706.x